Multi-Dimensional Flow-Preserving Compressed Sensing (MuFloCoS) for Time-Resolved Velocity-Encoded Phase Contrast MRI

Jana Hutter*, Peter Schmitt, Marc Saake, Axel Stübinger, Robert Grimm, Christoph Forman, Andreas Greiser, Joachim Hornegger, and Andreas Maier

***Abstract*—4-D time-resolved velocity-encoded phase-contrast MRI (4-D PCI) is a fully non-invasive technique to assess hemodynamics *in vivo* with a broad range of potential applications in multiple cardiovascular diseases. It is capable of providing quantitative flow values and anatomical information simultaneously. The long acquisition time, however, still inhibits its wider clinical use. Acceleration is achieved at present using parallel MRI (pMRI) techniques which can lead to substantial loss of image quality for higher acceleration factors. Both the high-dimensionality and the significant degree of spatio-temporal correlation in 4-D PCI render it ideally suited for recently proposed compressed sensing (CS) techniques. We propose the Multi-Dimensional Flow-preserving Compressed Sensing (MuFloCoS) method to exploit these properties. A multi-dimensional iterative reconstruction is combined with an interleaved sampling pattern (I-VT), an adaptive masked and weighted temporal regularization (TMW) and fully automatically obtained vessel-masks. The performance of the novel method was analyzed concerning image quality, feasibility of acceleration factors up to 15, quantitative flow values and diagnostic accuracy in phantom experiments and an *in vivo* carotid study with 18 volunteers. Comparison with iterative state-of-the-art methods revealed significant improvements using the new method, the temporal normalized root mean square error of the peak velocity was reduced by 45.32% for the novel MuFloCoS method with acceleration factor 9. The method was furthermore applied to two patient cases with diagnosed high-grade stenosis of the ICA, which confirmed the performance of MuFloCoS to produce valuable results in the presence of pathological findings in 56 s instead of over 8 min (full sampling).**

***Index Terms*—Compressed sensing, hemodynamics, magnetic resonance imaging (MRI), phase contrast MRI.**

Manuscript received July 23, 2014; accepted September 11, 2014. Date of publication September 19, 2014; date of current version January 30, 2015. *Asterisk indicates corresponding author.*

*J. Hutter is with the Pattern Recognition Lab, Friedrich-Alexander-Universität Erlangen-Nürnberg, 91058 Erlangen, Germany, and also with the School of Advanced Optical Technologies, 91058 Erlangen, Germany (e-mail: jana.hutter@cs.fau.de).

C. Forman, J. Hornegger, and A. Maier are with the Pattern Recognition Lab, Friedrich-Alexander-Universität Erlangen-Nürnberg, 91058 Erlangen, Germany, and also with the School of Advanced Optical Technologies, 91058 Erlangen, Germany.

P. Schmitt and A. Greiser are with the MR Application and Workflow Development, Siemens AG, Healthcare Sector, 91058 Erlangen, Germany.

M. Saake is with the Department of Radiology, University Hospital Erlangen, 91058 Erlangen, Germany.

A. Stübinger is with the Department of Vascular Surgery, University Hospital Erlangen, 91058 Erlangen, Germany.

R. Grimm is with the Pattern Recognition Lab, Friedrich-Alexander-Universität Erlangen-Nürnberg, 91058 Erlangen, Germany.

Color versions of one or more of the figures in this paper are available online at http://ieeexplore.ieee.org.

Digital Object Identifier 10.1109/TMI.2014.2359238

I. Introduction

THE ASSESSMENT of hemodynamics is important in the diagnosis of multiple cardiovascular diseases and is widely used for therapy decisions and planning. One example is the bi-lateral assessment of carotid flow to evaluate consequences of stroke or stenosis or flow patterns in aneurysms to assess the probability of ruptures. A further example is the assessment of severe internal carotid artery (ICA) stenosis, which can be done by measuring retrograde flow or the visualization of areas with very slow flow [1]. The requirements for clinically useful hemodynamic information include a good temporal resolution to observe the dynamics over the cardiac cycle and high spatial resolution in all three dimensions to assess even small arteries and to detect turbulence. Furthermore, the accuracy of clinically relevant parameters such as wall shear stress [2] or volumetric flow is highly dependent on the knowledge of anatomical vessel lumen and wall information.

Acquisition techniques for hemodynamic information include computed tomography angiography (CTA), Doppler ultrasound (DUS), fractional flow reserve (FFR) [3], and dynamic contrast-enhanced MRI (DCE-MRI), but they all come with significant drawbacks: CTA exposes the patient to ionizing radiation; FFR is highly invasive; DCE-MRI requires injection of a gadolinium-based contrast agent; and ultrasound is user-dependent and does not offer anatomical information [4]. In addition, Computational Fluid Dynamics is used to create simulations [5] based on patient-specific information such as heart rate and geometry [6]. But those cannot replace a fully patient specific *in vivo* acquisition of the blood flow velocities. 4-D PCI represents a fully noninvasive method to assess human blood flow. It provides furthermore intrinsically registered—as simultaneously acquired—anatomical and velocity information, enabling the calculation of a wide range of clinically relevant physiological parameters such as volumetric flow, peak velocity, and mean velocity [7].

A general drawback of this technique—if considerable 3-D coverage and high temporal and spatial resolution is required—is its long acquisition time, which originates from the synchronization to the cardiac cycle, the required segmented acquisition technique and the velocity encoding. The acquisition time for a full scan of the carotid bifurcation region for a reasonable parameter set offering both good spatial and temporal resolution reaches up to 30 min.

Recently, approaches to reduce acquisition time for 4-D PCI have been proposed: They rely either on optimized encoding strategies [8], [9] or on specific reconstruction strategies able to reconstruct the output volumes from highly undersampled k-space data. Sampling below the Nyquist criteria leads to significant image artifacts which are addressed by specific reconstruction techniques. One group of methods consists of pMRI such as GRAPPA [10] and SENSE [11]. The spatially varying information of multiple coils around the subject which acquire k-space data simultaneously is used to reduce the scan time. The additional spatial sensitivity information of the coil setup is exploit to reconstruct images from undersampled k-space data. pMRI techniques are employed for dynamic 4-D PCI often in combination with temporal encoding schemes such as kt-GRAPPA [12] or compartment-based kt-SENSE [13]. Non-Cartesian trajectories such as spirals in combination with SENSE were introduced by Steeden *et al.* [14]. A different group of methods, able to reconstruct even higher accelerated data, are iterative reconstruction techniques and recently proposed compressed sensing (CS) techniques [15], [16] which are frequently combined with pMRI methods. CS relies on generating noise-like artifacts by using incoherent samplings, which can be separated from image information using adapted regularization. The basis for the employed regularizers are sparsity or transfer sparsity assumptions, The resulting optimization problem, combining the fidelity to the measured data with regularization terms is solved using nonlinear reconstruction algorithms. This technique is promising for 4-D PCI as the fundamental principles of incoherence and sparsity are applicable. Incoherence is achieved by choosing dedicated sampling trajectories for the acquisition in k-space. Those are either Cartesian or non-Cartesian. Non-Cartesian trajectories such as radial or spiral sampling offer higher flexibility compared to Cartesian patterns with regard to incoherence. But this benefit is associated with the required additional gridding step [17] as major drawback which significantly adds to the computational effort of the iterative reconstruction. It was shown that the theoretical best choice, randomized patterns, is less suitable for highly accelerated MRI. The central k-space region, containing low frequencies requires denser sampling to achieve good results [18]. Furthermore, high acceleration randomized patterns can result in significant gaps between the samples. Proposed alternatives include pseudo-random or Poisson-distributed sampling [19]. Sparsity is inserted into the CS formulation with specific regularizers, varying between very general assumptions about medical images such as a certain smoothness and the possibility to be expressed by a low number of Wavelet coefficients and very acquisition specific constraints. These include for 4-D PCI, complex difference sparsity as shown by Kwak [20], divergence-free constraints described by Busch *et al.* [21] and specific phase regularization [22]. Furthermore, the dynamic character of 4-D PCI is exploited by Kim *et al.* [23], proposing a kt SPARSE SENSE approach reconstructing jointly reference and velocity-encoded data using a temporal FFT and PCA as sparsifying transform. Velikina *et al.* [24] include second order temporal differences. Spatially varying temporal constraint regularization has been applied to PC MRI by Hulet *et al.* [25]. Acceleration methods based on CS further include work by Joseph *et al.*, who showed good results applying nonlinear inverse reconstruction techniques [26] and the recent work by Santelli *et al.* extending the L1-spirit method to PCI data [27]. The only studies applying CS methods to *in vivo* carotid PCI data were presented by Tao *et al.* [28] introducing temporal Fourier transform in combination with uniformly random sampling and by Hutter *et al.* [29] using a Low-Rank Sparsity assumption. Carotid PCI data is challenging due to the small vessel diameter, the highly pulsatile flow and the complex flow behaviour around the bifurcation. For carotid PCI, the dynamic changes originate mainly from blood flow effects, either directly or indirectly by vessel wall motion due to its pulsatile nature. In addition, their spatial extent is limited to the vessel proximity. Further possible origins of movement, patient-, cardiac-, and breathing motion can be neglected for this application. The temporal resolution of derived physiological parameters with clinical relevance, such as volumetric flow, peak velocity, or wall shear stress depends to a high degree on the temporal fidelity of the flow reconstruction. A well-suited temporal regularization should thus exploit the anatomical correlation in the static tissue parts to offer volumes with clinically accepted image quality while maintaining the temporal fidelity in vessel proximity. Two basic requirements exist for the usage of this prior knowledge: The first requirement is a joint reconstruction algorithm which reconstructs all volumes for all time steps as well as velocity encodings simultaneously to allow for exploiting correlations spanning over different images along all dimensions. Secondly, a stable dynamic sub-division of the image volume into vessels and static tissue is required. The necessary information for this subdivision is intrinsically available in 4-D PCI with the anatomical reconstruction. The Multi-dimensional Flow-adapted Compressed Sensing algorithm (MDFCS) used this information as prior in combination with a dedicated pattern and iterative reconstruction [30]. In this work, we extend this approach to a fully interleaved and incoherent sampling (I-VT) strategy, enabling higher acceleration through fully internally shared calculation of the coil profiles. The adaptive TMW regularization strategy is refined by adding additional weighting and masking with a static and dynamic mask for a stable and automatic differentiation into static and nonstatic tissue during the reconstruction. The resulting Multi-Dimensional Flow-preserving Compressed Sensing (MuFloCoS) algorithm exploits the significant spatio-temporal correlation in the dynamic acquisition while preserving the temporal flow resolution. The adaptive masking strategy relies on inherent 4-D PCI features, which are made accessible by an interleaved sampling scheme in the temporal and velocity encodings (I-VT). In summary, in contrast to other methods, not only the spatial and temporal dimension, but also the 4-D PCI inherent velocity encoding dimension is included in all steps of the algorithm. The TMW regularization penalizes nonsimilarity to neighboring temporal phases but differentiates between static and flow affected areas using adaptive vessel masks in order not to introduce temporal blurring. The paper is structured as follows. The acquisition and reconstruction basics as well as the postprocessing of the image data for PCI are introduced, the novel MuFloCoS method is described as well as the experimental setup consisting of a

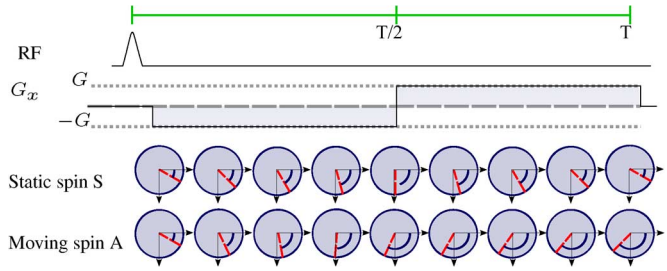

Fig. 1. Static magnetization S and moving magnetization A under the influence of the bipolar gradient $G(t)$ in the acquisition time $[0, T]$.

phantom experiment, a larger carotid volunteer study with 18 subjects and two patient cases. Image based quantitative measures as well as physiological parameters were calculated and used to evaluate the accuracy of the proposed method. The novel method is compared against the fully sampled reference as well as different CS methods such as L1 regularized SENSE, kt-SPARSE SENSE once with temporal Fourier transform and once with temporal principal component analysis (PCA), the method proposed by Tao *et al.* 2013 [28] and MDFCS. Another experiment shows the stability and acceleration capacities of MuFloCoS. Finally, the results of the two patient cases of severe stenosis of the ICA, accelerated and reconstructed with MuFloCoS, are presented.

II. 4-D PCI Theory

The magnetic field in an MRI measurement consists of a homogeneous magnetic field B_0 and a gradient field B_G, generated from gradients in all spatial dimensions which are switched during the measurement sequence. Phase Contrast MRI relies on the linear dependency of the signal phase from velocity in presence of special bipolar gradients $G(t)$ consisting of two lobes with the same amplitude G but opposite polarity. The total field considering a gradient $G_x(t)$ in x-direction equals to $B(x,t) = B_0 + G_x(t) = B_0 + x(t)G(t)$. The accumulated phase at the end of an acquisition interval $[0, T]$ is calculated by integrating the frequency over the time and using the Larmor frequency γ as

$$\phi(x) = \int_0^T \gamma B_0 + \gamma x(t) G(t) dt. \tag{1}$$

The mechanism to obtain velocity information utilizing the signal phase is illustrated observing two spins with different velocities (see Fig. 1). If a magnetization S is static, $x(t) = x_0\ \forall t$ and magnetization A is moving along the direction of the gradient with constant velocity v_1, its time-dependent position equals $x(t) = x_0 + v_1 t$.

During the first slope for $t \in [0, T/2]$, the transverse magnetization of both spins is de-phased. The second slope re-phases the static magnetization, leading to a net phase change of 0. Magnetization A, however, during its movement experiences different magnetic field conditions and is not completely re-phased during the second slope of the gradient. As a result, a term including the first gradient moment and providing a linear dependency on the velocity is obtained

$$\begin{aligned}
\phi_1^S(x) &= \int_0^T \gamma B_0 + \gamma x_0 G(t) dt = \gamma B_0 T \\
\phi_1^A(x) &= \int_0^T \gamma B_0 + \gamma (x_0 + s_1 t) G(t) dt \\
&= \gamma B_0 T + \gamma G \left(\int_0^{\frac{T}{2}} x_0 dt - \int_{\frac{T}{2}}^T x_0 dt + v_1 \int_0^{\frac{T}{2}} t dt \right. \\
&\qquad \left. - v_1 \int_{\frac{T}{2}}^T t dt \right) \\
&= \gamma B_0 T - v_1 \gamma G \left(\frac{T}{2} \right)^2 .
\end{aligned}$$

To obtain a linear relation between the velocity and the measured phase as well as to compensate for phase effects unrelated to flow such as field inhomogeneties an additional velocity-compensated reference acquisition is required. For 3-D velocity information, most 4-D PCI sequences use a 4-point velocity encoding scheme [31], which requires one flow-compensated reference scan and three velocity sensitive scans [32] in through-plane, anterior-posterior and right-left direction. Dynamic information over the cardiac cycle is obtained by triggering the acquisition to the R-wave in the cardiac cycle of the patient using electrocardiogram (ECG) or pulse triggering. N_t time steps are defined starting from the R-wave, within which subsets of k-space data are collected over multiple heart beats in a segmented acquisition scheme.

A. Reconstruction

For the following, $\mathbf{x}$ will be the column wise written notation for a matrix $\mathbf{X}$. The variables N_t and N_s denote the number of temporal phases and velocity encodings, $N_p = N_s N_t$ represents the problem size. $N_k = N_{k_x} N_{k_y} N_{k_z}$ is the number of k-space samples, N_c the number of parallel receive coils and $N = N_x N_y N_z$ the image volume size.

For each temporal phase t, each velocity encoding s, and each channel γ, one k-space vector $\mathbf{m}_\gamma^{t,s} \in \mathbb{C}^{N_k}$ is acquired. The set of all N_c k-space acquisitions corresponding to the same temporal phase and velocity encoding are represented as the all-channel vector $\mathbf{m}^{t,s} \in \mathbb{C}^{N_k N_c}$. For each time step, vectors $\mathbf{m}^t = [\mathbf{m}^{t,1} \dots \mathbf{m}^{t,N_s}]^T \in \mathbb{C}^{N_k N_c N_s}$ are created, which form the total raw data vector $\mathbf{m} = [\mathbf{m}^1 \dots \mathbf{m}^{N_t}]^T \in \mathbb{C}^{N_k N_c N_p}$.

The reconstruction leads to the N_p image space vectors $\mathbf{x}^{t,s} \in \mathbb{C}^N$. The image space vector $\mathbf{x} \in \mathbb{C}^{N N_p}$ is formed analogously.

Transformation between image space and k-space is done via the system matrix $\mathbf{E} \in \mathbb{C}^{N_k N_c N_p \times N N_p}$ assembled of matrices $\mathbf{E}^{t,s} \in \mathbb{C}^{N_k N_c \times N}$, such that $\mathbf{E}\mathbf{x} = \mathbf{m}$ and $\mathbf{E}^{t,s}\mathbf{x}^{t,s} = \mathbf{m}^{t,s}$

$$\mathbf{E} = \begin{pmatrix} \mathbf{E}^1 & & 0 \\ & \ddots & \\ 0 & & \mathbf{E}^{N_t} \end{pmatrix} \text{ with } \mathbf{E}^t = \begin{pmatrix} \mathbf{E}^{t,1} & & 0 \\ & \ddots & \\ 0 & & \mathbf{E}^{t,N_s} \end{pmatrix}. \tag{2}$$

For conventional fully sampled single-channel MRI, the system matrix $\mathbf{E}$ consists of Fourier coefficients. For pMRI, the matrices $\mathbf{E}^{t,s}$ include the coil sensitivity profiles $\mathbf{c}_\gamma^t$ and the Fourier coefficients [11]. Direct solution of $\mathbf{Ex} = \mathbf{m}$ is impossible in the highly accelerated case as the system is heavily under determined for $N_k < N$.

B. Extraction of Flow-Related and Anatomical Information

The reconstructed data sets $\mathbf{x}^{t,s}$ are further processed to obtain both anatomical information and quantitative 3-D velocity information. For the case of three-directional velocities, N_s equals four. The complex difference between velocity-compensated and velocity-encoded acquisitions highlights the regions with moving magnetization by subtracting out the static regions, corresponding to moving protons. It can therefore be used to obtain angiographic images which highlight the vessel anatomy. Respective complex differences are calculated for all velocity encoding directions. The sum of their magnitudes results in the angiographic image $\mathbf{a}^t \in \mathbb{C}^N$, providing high contrast for areas with flow irrespective of the direction. The quantitative information is obtained via the signal phase difference between velocity-compensated and encoded image for each flow encoding direction $s = 2, \ldots, N_s$ as $\mathbf{p}^{t,s} \in \mathbb{C}^N$. Calculations of $\mathbf{a}^t$ and $\mathbf{p}^{t,s}$ are performed as

$$a_\iota^t = \sqrt{\sum_{s=2}^{s} \left(x_\iota^{t,1} - x_\iota^{t,s} \right)^2} \quad p_\iota^{t,s} = \arg\left(x_\iota^{t,s}\right) - \arg\left(x_\iota^{t,1}\right). \tag{3}$$

The phase in $\mathbf{p}^{t,s}$ is encoded to values within the interval $[-\pi, \pi]$, which can lead to wrapping artifacts and misinterpretation of flow exceeding this range as slow flow in the opposite direction. In order to avoid those artifacts, the velocity encoding parameter, also called venc, ν, is chosen as the maximum expected velocity in each flow encoding direction. Finally, 3-D velocity fields $\mathbf{v}^{t,s} \in \mathbb{C}^{3\times N}$ are obtained as $\mathbf{v}^{t,s} = (\nu/\pi)\mathbf{p}^{t,s}$.

III. MuFloCoS

The novel MuFloCoS approach is presented in detail here. Four main points are in the focus: the interleaved I-VT pattern is explained in Section III-A; the multi-dimensional joint iterative Newton-based reconstruction in Section III-B; the vessel-masked and temporal weighted TMW regularization in Section III-C and finally the domain sub-division using the anatomical image detailed in Section III-D. Furthermore, the choice of all parameters is given along with pseudo-code and a schematic flowchart.

A. The I-VT Sampling Strategy

The sampling for 4-D PCI can be varied in four dimensions, two intra-volume and two inter-volume directions. The intra-volume degrees of freedom are k_y and k_z direction. The acquisition in the read-out direction k_x is substantially faster than the phase encoding directions k_y and k_z as no gradient switches are required. The inter-volume directions are the time t and the flow encoding direction s. While state-of-the-art approaches typically offer k_y, k_z and t-direction variation, the freedom in flow encoding direction s is rarely used. The MuFloCoS algorithm relies on a Cartesian pattern, which can be analytically calculated while offering both a substantial amount of incoherence and suitability for high acceleration factors. The omission of a gridding step, possible through the use of a Cartesian pattern, in every iteration reduces the computational effort, and therefore the reconstruction time. The pattern is described by $u_{\boldsymbol{\kappa}}^{t,s}$, with $\boldsymbol{\kappa} = (\kappa_x, \kappa_y, \kappa_z)$, it equals "1" for sampled points and "0" for omitted k-space samples. The generation of the pattern for all time steps t and flow encodings s is detailed in the following. Intra-volume directions are exploited by separating k-space into a central region $\mathcal{C}$, which is regularly under-sampled and has the dimension $N_{\kappa_{cy}} \times N_{k_{cz}}$, and a peripheral region, $\mathcal{P}$ sampled irregularly with decreasing density following an inverse root function [33]. The center is described by the spacing $\mathbf{d_c}$, fixed to N_s for the 2-D version and $[N_s/2, N_s/2]$ for 3-D, and the offset $\mathbf{o}_c(j(t,s))$, obtained as result of the mapping $j(t,s)$. Fig. 2(a) illustrates the center sampling patterns for $j = 1, \ldots, N_s$ with $N_s = 4$. Conventional temporal approaches without s-variations can be modelled with $j_T(t,s) = c(t)$, where c depends uniquely on t. Two alternatives including s-Variations for the mapping function are proposed, regular permutations $j_P(t,s) = tN_s + s$ and random shifting $j_T(t,s)$, obeying two constraints: 1) two subsequent time steps in the same velocity encoding never share the same central lines and 2) all k-space central lines must be sampled in each time step

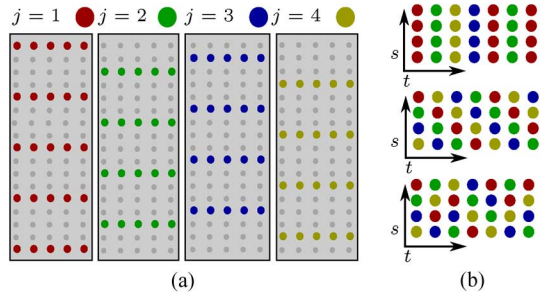

Fig. 2. (a) Schematic 2-D illustration of central k-space variations. (b) Mapping of time steps t and velocity encodings s for three different mapping functions $j(t,s)$: Temporal variations $j_T(t,s)$, regular $j_P(t,s)$, and random permutations $j_R(t,s)$.

$$j_R(t,s) = \text{rand}\left([1,\ldots,s]\right) \text{ such that} \tag{4}$$
$$(I)\ j_R(t_i,s) \neq j_R(t_k,s) \text{ for } |t_i - t_k| = 1 \text{ and} \tag{5}$$
$$(II)\ j_R(t,s_i) \neq j_R(t,s_k) \quad \forall s_i, s_k \in \{1,\ldots,s\}. \tag{6}$$

The same offset is used for the start of k-space peripheral inverse root sampling, using a parametrizable quadratic function $s(i,(a,b))$ to determine the distance between successive sampling points.

The results for all three mentioned mapping functions are illustrated in Fig. 2(b) for $j_T(t,s)$ on the top, for $j_R(t,s)$ in the middle and for $j_P(t,s)$ on the bottom. The corresponding patterns including peripheral inverse root sampling are shown in Fig. 3 with their point spread functions. The higher peak-to-sidelobe-ratio in the I-VT variants in three illustrates the higher

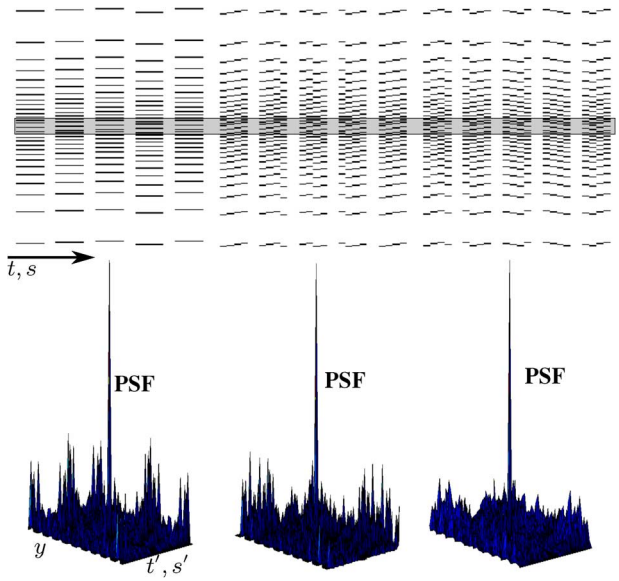

Fig. 3. Exemplary patterns for 2-D sampling with $N_{k_y} = 256$ for the three mentioned mapping functions with the corresponding point spread functions PSF $((t', s'), y)$ using the same scaling illustrate the better peak-to-side lobe ratio for the random permutations.

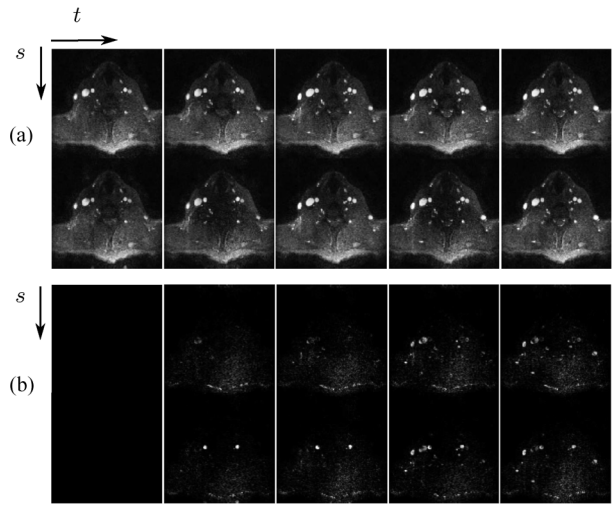

Fig. 4. Illustration and justification of the weighted and masked temporal regularization strategy. (a) Magnitude of the flow-compensated and through-plane encoded images is shown for $t \in \{1 \dots 5\}$. (b) Finite differences over time between the images for $t = 1$ and $t_j \in \{2 \dots 5\}$ are depicted.

incoherence of the under sampling artefacts, which is an important prerequisite for CS. The proposed I-VT sampling strategy exploits s and t direction to add incoherence, but also to enable two additional features.

- The pattern, interleaved in s and permuted in t-direction, allows the calculation of approximate static and dynamic anatomical images $\mathbf{a}$, which are used later in the algorithm for the anatomy-based sub-division (Section III-D).
- Instead of acquiring the coil profiles in a separate time-consuming external scan, they can be obtained by combining central k-space lines over the N_s velocity encodings. The combined fully sampled low resolution k-space is filtered with a Hanning window [11].

B. Multi-Dimensional Iterative Newton-Based Reconstruction

In contrast to the conventional case, where each volume is reconstructed individually, the approach combines the raw data of all phases and velocity encodings in one reconstruction. This is favourable over individual reconstruction, as it enables the use of sparsifiying transforms spanning over different images along all dimensions to exploit similarities during the reconstruction. The objective function for the iterative reconstruction consists of a data fidelity term $D(\mathbf{x})$ and the regularization term $R(\mathbf{x})$. The data fidelity term

$$D(\mathbf{x}) = \frac{1}{2}\|\mathbf{E}\mathbf{x}^i - \mathbf{m}\|_2^2 \tag{7}$$

includes the raw data and the pMRI reconstruction matrix $\mathbf{E}^{t,s} = (e^{t,s}_{c\kappa,\iota}) \in \mathbb{C}^{N_c N_k \times N}$ including the Fourier coefficients, the under sampling pattern $\mathbf{u}^{t,s}$ and the coil profiles described by $\mathbf{c}^{t,\gamma}$

$$e^{t,s}_{\gamma\kappa,\iota} = u^{t,s}_{\kappa} e^{i k^{t,s}_{\kappa} r_\iota} c^{t,\gamma}_{\iota}. \tag{8}$$

Thereby r_ι is the position of voxel ι in image space, $k^{t,s}_{\kappa}$ is the frequency. A more detailed description of the regularization term $R(\mathbf{x})$ is found in Section III-C.

C. Vessel-Masked and Temporal Weighted L_1 Regularization

The MuFloCoS approach proposes an adaptive vessel-masked and weighted temporal regularization (TMW) which exploits spatio-temporal correlation while maintaining the temporal flow fidelity using the anatomy-based sub-division. The significant spatio-temporal correlations of PCI can be observed in the first five time steps for the velocity compensated (upper row) and one of the velocity encoded scans (lower row). Those can be modelled using finite differences (FD) ∇_t with different step length in time direction. For each temporal time point t and encoding s, the FD $\nabla_t^{t,s,t_j}\mathbf{x} \in \mathbf{C}^N$ to phase t_j with $j \in [1, \dots, N_t], t_j \neq t$ is calculated voxel wise as

$$\left(\nabla_t^{t,s,t_j}\mathbf{x}\right)_\iota = x_\iota^{t_j,s} - x_\iota^{t,s}. \tag{9}$$

Fig. 4(b) illustrates $\nabla_t^{t,s,t_j}\mathbf{x}$ for $t = 1$ and $t_j \in \{2 \dots 5\}$ for the velocity compensated $(s = 1)$ and encoded $(s = 2)$ data scans. To assess the proposed sparsity assumption as well quantitatively, the coefficients of the FD images $|(\nabla_t^{t,s,t_j}\mathbf{x})_\iota|$ for $\iota \in \{1 \dots N\}$ are sorted by magnitude in Fig. 5 for $\nabla_t^{1,1,2}\mathbf{x}$, $\nabla_t^{1,1,4}\mathbf{x}$, $\nabla_t^{1,2,2}\mathbf{x}$, and $\nabla_t^{1,2,4}\mathbf{x}$. Three observations can be derived and will motivate the algorithmic choices detailed below. In general, it can be well observed, that the significant high contributions are concentrated within few pixels in the coefficient plot. This is illustrated in the difference images in Fig. 4(b), where the main contributions to the finite differences clearly are concentrated at the vessels, which show the meaningful velocity changes over time, while the background has relatively low contribution. There is a substantial difference between the flow compensated and encoded images. While the flow-encoded scans show the described enhancement of vessels, this is less clearly observable in the compensated scans. The zooms into the

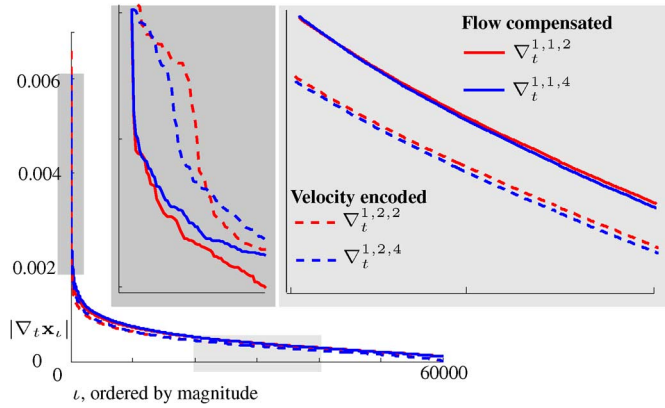

Fig. 5. Finite difference coefficients $|(\nabla_t^{t,s,t_j}\mathbf{x})_\iota|$ ordered by magnitude show the sparsity of the used differences for $t_j = 2$ and $t_j = 4$.

highest 0.1% of the coefficients show a more significant contribution of the velocity-encoded scans (dotted lines). The zoom into the lower coefficients reveals the inverse situation. In summary, the coefficients for the flow-encoded scans are more compressed in the highest values. Finally, the concentration of contributions to the vessels decreases for larger time steps. However, the general importance of the differentiation in vessels and background stays valid for a certain range of subsequent time steps. Based on those observations, the MuFloCoS algorithm includes three features into the temporal finite difference regularization:

- a vessel-mask limiting the regularization to background areas to preserve the dynamics within the vessels,
- different treatment for the flow compensated and velocity encoded scans, and finally
- a temporal weighting in time direction, attributing higher importance to closer time steps.

The difference terms are arranged for all step sizes in a common vector $\nabla_t^{t,s}\mathbf{x} \in \mathbf{C}^{NN_t}$

$$\nabla_t^{t,s}\mathbf{x} = \begin{pmatrix} \nabla_t^{t,s,1}\mathbf{x} \\ \cdots \\ \nabla_t^{t,s,N_t}\mathbf{x} \end{pmatrix} \tag{10}$$

and finally for all flow encodings to $\nabla_t^t\mathbf{x} \in \mathbf{C}^{NN_p}$ and all time steps to $\nabla_t\mathbf{x} \in \mathbf{C}^{NN_pN_t}$

$$\nabla_t\mathbf{x} = \begin{pmatrix} \nabla_t^1\mathbf{x} \\ \vdots \\ \nabla_t^{N_t}\mathbf{x} \end{pmatrix} \text{ with } \nabla_t^t\mathbf{x} = \begin{pmatrix} \nabla_t^{t,1}\mathbf{x} \\ \vdots \\ \nabla_t^{t,N_s}\mathbf{x} \end{pmatrix}. \tag{11}$$

The weighting function $w(t,t_j)$ is realized either with a box function $w_B(t,t_j)$ or with a Gaussian kernel $w_G(t,t_j) = (-1/\sqrt{2\pi})e^{-((t_j-t)^2/\sigma^2)}$, centred at the position t with standard deviation σ, determining the extent of the influence of neighboring phases. Thereby the vector $\mathbf{w}^t \in \mathbb{R}^{N_t}$ equals $\mathbf{w}^t = [w(t,1)\ldots w(t,N_t)]$. It is used to form the weighting matrix for time step t $\mathbf{W}^t \in \mathbb{R}^{NN_s\times NN_p}$ as well as the complete weighting matrix $\mathbf{W} \in \mathbb{R}^{NN_p\times NN_pN_t}$

$$\mathbf{W} = \begin{pmatrix} \mathbf{W}^1 & & \\ & \ldots & \\ & & \mathbf{W}^{N_t} \end{pmatrix} \text{ with } \mathbf{W}^t = \begin{pmatrix} \mathbf{w}^t & & \\ & \ldots & \\ & & \mathbf{w}^t \end{pmatrix}. \tag{12}$$

Finally, the vessel masks $\mathbf{b}^t \in \mathbf{R}^N$ are involved. Those theoretically equal to $b_\iota^t = 1$ for voxels within a vessel and $b_\iota^t = 0$ for background voxels, for practical reasons nonbinary values $\in [0,1]$ are chosen. Their calculation is detailed in Section III-D. To limit the regularization to the background areas, the masks are subtracted from the unity vector $\mathbf{1}_N - \mathbf{b}^t$, such that voxels within vessels are multiplied with "0" and do not contribute to the value of the regularization. The differentiation between compensated and encoded acquisitions is modelled by weighting all voxels of the compensated scan with "1," meaning, that the regularization operates on them.

The masks are arranged in the diagonal matrices $\mathbf{B}^t = \mathrm{diag}(\mathbf{b}^t) \in \mathbf{R}^N$, and composed to form matrices $\mathbf{M}^t \in \mathbf{R}^{NN_s\times NN_s}$. These are used in the assemblage of the final entire mask matrix $\mathbf{M} \in \mathbf{C}^{NN_p}$

$$\mathbf{M} = \begin{pmatrix} \mathbf{M}^1 & & \\ & \ddots & \\ & & \mathbf{M}^{N_t} \end{pmatrix} \text{ with}$$

$$\mathbf{M}^t = \begin{pmatrix} \mathbf{1} & & \\ & \mathbf{1}-\mathbf{B}^t & \\ & \ddots & \\ & & \mathbf{1}-\mathbf{B}^t \end{pmatrix}. \tag{13}$$

The temporal differences $\nabla_t\mathbf{x}$ are multiplied with the mask matrix $\mathbf{M}$ and the weighting matrix $\mathbf{W}$

$$R(\mathbf{x}) = \|\mathbf{MW}\nabla_t\mathbf{x}\|_{L_1}. \tag{14}$$

The objective function including the regularization weight λ_{tmw} equals

$$\mathcal{L}(\mathbf{x}) = \underbrace{\frac{1}{2}\|\mathbf{Ex}-\mathbf{m}\|_{L_2}^2}_{\text{Data fidelity term}} + \underbrace{\lambda_{\mathrm{tmw}}\|\mathbf{MW}\nabla_t\mathbf{x}\|_{L_1}}_{\text{Regularization}}. \tag{15}$$

This is solved iteratively by

$$\hat{\mathbf{x}} = \arg\min_{\mathbf{x}} \mathcal{L}(\mathbf{x}). \tag{16}$$

D. Anatomy-Based Sub-Division

During the iterative reconstruction the volume, defined by its voxel set ι_V with voxel indices $\iota \in \{1\ldots N\}$, is divided into a static part consisting of the voxel set ι_S and a part affected by flow motion ι_M with $\iota_V = \iota_S \cup \iota_M$ to allow guidance of the temporal regularization to the static parts. This is important to avoid temporal blurring. The goal is therefore to obtain dynamic masks $\mathbf{b}^t \in [0,1]^N$ with the theoretical property

$$b_\iota^t = \begin{cases} 1 & \text{if } \iota \in \iota_M \text{ and} \\ 0 & \text{if } \iota \in \iota_S. \end{cases} \tag{17}$$

As the subdivision correlates mainly with the vessel anatomy in the chosen application, b_ι^t is referred to as vessel mask. The selected differentiation feature is the occurrence of flow as it is inherent in the PCI technique through the anatomical images $\mathbf{a}^t$ as explained in Section II-B. The proposed interleaved and incoherent pattern leading to distributed incoherent artifacts in s and t direction allows an approximation of $\mathbf{a}^t$, which is used to generate the masks $\mathbf{b}^t$. This information is then available for

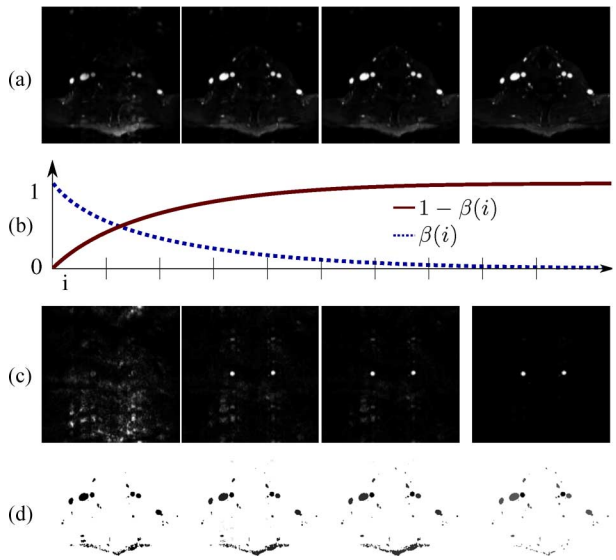

Fig. 6. Generation of the vessel masks as a combination of the static and dynamic anatomical images is illustrated. The (a) static images $\bar{\mathbf{a}}$ and (c) dynamic images $\check{\mathbf{a}}^t$ for the first three and the last iteration are depicted. (c) Evolution of their respective influence is shown depending on the parameter $\beta(i)$. (d) Final vessel masks $\mathbf{b}^t$ for $t = 2$ are visualized.

the temporal regularization and directs it to the known locations of correlation. Beside the approximation of the typical PCI anatomical map $\check{\mathbf{a}}^t$, as described in (3), a static approximation $\bar{\mathbf{a}}$ calculated as the anatomical image over all phases is used

$$\bar{a}_\iota = \sqrt{\sum_{s=2}^{s} \frac{1}{N_t} \left(\sum_{t=1}^{N_t} (\mathbf{x}^{t,1})_\iota - \sum_{t=1}^{N_t} (\mathbf{x}^{t,s})_\iota \right)^2}. \quad (18)$$

During the reconstruction, both are calculated based on the actual image estimate $\mathbf{x}_i^{t,s}$ for iteration $i = 1, \ldots, N_i$. The first necessary estimate used during the first iteration, referred to by $\mathbf{x}^0$ corresponds to the conventionally reconstructed raw data vector using the Sum-of-Squares [34] method: $\mathbf{x}^0 = \mathcal{S}(\mathbf{m})$. By updating the masks in each iteration, the algorithm adapts to the improving reconstruction quality. MuFloCoS uses a combination of both static and dynamic image, which is crucial for the stability and robustness of the algorithm particularly for the first iterations which are heavily influenced by aliasing artefacts. This is illustrated with a 9.0 times under-sampled data set in Fig. 6. The obtained static masks for the first four iterations and the last iteration are shown in Fig. 6(a), the dynamic images for time step 2 in Fig. 6(c). The aliasing artefacts in the first dynamic masks are visible, while the static images allow clear depiction of the vessels from the first iteration on. This is possible through the use of the I-VT pattern with variations in both directions, used combined to generate the anatomical images.

The sub-division is entirely based on this intrinsically obtained anatomical images $\bar{\mathbf{a}}$ and $\check{\mathbf{a}}^t$ by applying a binary threshold l. The obtained binary masks $\bar{\mathbf{b}}^i$ and $\check{\mathbf{b}}^i$ for voxel ι equal

$$\bar{b}_\iota^{\,i} = \begin{cases} 1 & \text{if } \bar{\mathbf{a}}_\iota^t > l \\ 0 & \text{if } \bar{\mathbf{a}}_\iota^t \leq l \end{cases} \text{ and } \check{b}_\iota^{\,i} = \begin{cases} 1 & \text{if } \check{\mathbf{a}}_\iota^t > l \\ 0 & \text{if } \check{\mathbf{a}}_\iota^t \leq l \end{cases}. \quad (19)$$

The influence of the static and dynamic anatomical image approximation changes smoothly with the parameter $\beta(i)$ depending only on the iteration step i with

$$\mathbf{b}^t = \frac{1}{2} \left(\beta(i) \bar{\mathbf{b}} + (1 - \beta(i)) \check{\mathbf{b}}^t \right), \text{ with } \beta(i) = 1/i^\gamma. \quad (20)$$

The evolution of $\beta(i)$ over iteration steps is visualized in Fig. 6(b). Fig. 6(d) illustrates the final masks $\mathbf{b}^t$.

E. MuFloCoS Implementation Details

This section describes the details of the MuFloCoS algorithm implementation. The algorithm was included into a C++ reconstruction framework, offering both a linked version to the MR scanner and a standalone version for testing purposes. The linked version directly processes the raw data after acquisition using the inline data processing pipeline. The MuFloCoS algorithm seeks to find a solution $\tilde{\mathbf{x}}$ for the problem as stated in (15).

Algorithm 1: MuFloCoS algorithm

Require: $\mathbf{m}, \mathbf{u}, \mathcal{L}, \nabla\mathcal{L}$

Require: $w(t, t_j), \epsilon, \lambda_{\text{tmw}}, N_i, \beta(i)$

1: Calculate combined coil profiles $c^t_{(\gamma,\kappa)}$

2: Obtain direct reconstruction with $\mathcal{S}\mathbf{m}^{t,s}$

3: Calculate $\bar{\mathbf{a}}^t$ and $\bar{\mathbf{b}}^t$

4: Initialize mask matrix $\mathbf{M}$

5: Assemble weighting matrix $\mathbf{W}$

6: Assemble encoding matrix $\mathbf{E}$ with $e^{t,s}_{\gamma\kappa,\iota} = u^{(t,s)}_\kappa e^{ik^{t,s}_\kappa r_\iota} c^t_{(\gamma,\kappa)}$

7: **while** $i < N_i$ **do**

8: Newton update evaluating the objective function $\mathcal{L}$ as follows:

9: Calculate the data fidelity term $D(\mathbf{x}) = (1/2)\|\mathbf{E}\mathbf{x}^i - \mathbf{m}\|_2^2$

10: Assemble FD vector $\nabla^t = [\nabla_t^1 \ldots \nabla_t^{N_t}]$

11: Calculate $R(\mathbf{x}) = \|\mathbf{M}\mathbf{W}\nabla_t\mathbf{x}\|_{L_1}$

12: Update $\mathbf{x}^{i+1}$

13: Update $\bar{\mathbf{a}}, \check{\mathbf{a}}^t, \bar{\mathbf{b}}, \check{\mathbf{b}}^t$

14: Combine $\bar{\mathbf{b}}$ and $\check{\mathbf{b}}^t$ to $\mathbf{b}^t$ using $\beta(i)$

15: Update mask matrix $\mathbf{M}$

16: **end while**

17: **return** $\mathbf{x}$

The complete MuFloCoS algorithm is represented in the flow chart in Fig. 7 as well as in a detailed step overview in algorithm 1. The preprocessing in steps 1–6 includes shared coil profile calculation, initialization of the vessel mask, calculation of the temporal weights and assembling of the encoding matrix. Then, the iterative process is started.

Considering the size of the optimization problem with NN_p unknowns, a limited-memory BFGS solver [35] is used, which

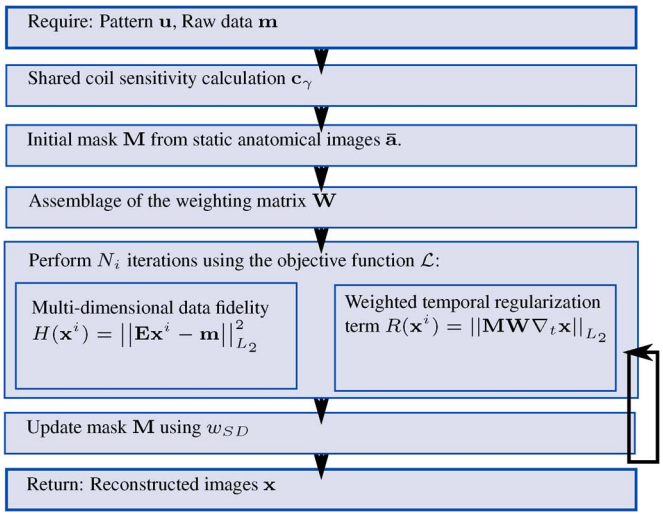

Fig. 7. Scheme of the MuFloCoS algorithm.

proved to be memory-efficient and stable. Replacement with further solvers such as the conjugate gradient method is possible without introducing structural changes. For all gradient-based solvers, both the objective function and its gradient are required within each iteration. Finally, the vessel mask matrix is updated.

The parameters for MuFloCoS were chosen equal for all datasets and experiments as $l = 0.1 \max_t \bar{a}_t$, $\sigma = 1.8$ and $\lambda_{\mathrm{tmw}} = 0.004$. The $\epsilon = 0.001$ ensures computational efficiency, as the differences are calculated only in the relevant kernel $\mathrm{supp}(w)$.

IV. Experiments and Results

A. Phantom Experiment

Phantom data was acquired using an MR compatible pump (CardioFlow 5000 MR, Shelley Medical, Toronto, Canada) connected to a control unit outside the scanner room and a tube system filled with blood mimicking fluid. An inflow–outflow setup was used for this study with two connected tubes of diameter 1.9 cm and a phantom bottle to simulate tissue contrast. The imaging volume plane was chosen orthogonal to the tubes, such that each imaging plane contained a cross section of the bottle and both the in- and outflow tube. See Fig. 8(a) for a schematic representation of the setup. A regulated laminar flow with 150 ml/s was pumped through the tube system and imaged on a 3T MR scanner (MAGNETOM Skyra, Siemens Healthcare Sector, Erlangen, Germany). The imaging parameters were FOV 190 × 130 mm, matrix 256 × 176 and a slice thickness of 3.1 mm, $\mathrm{TE/TR} = 3.4/6.2$ ms, temporal resolution 49.6 ms and flip angle 20°. The controlled setup allows to verify the flow conservation law between in- and outflow (Q_i, Q_o) in each slice D_{io}, and between adjacent slices regarding the inflow D_{si} and the outflow D_{so}

$$\mathbf{D_{io}} = \frac{|Q_i - Q_o|}{|Q_i|} \quad \mathbf{D_{si/so}} \frac{|Q_{si/o} - Q_{si/o-1}|}{|Q_{si/o}|}. \tag{21}$$

The fully sampled data sets were reconstructed with the conventional Sum-of-Squares (SoS) technique to obtain a reference volume. The I-VT pattern with acceleration factor 9 was applied

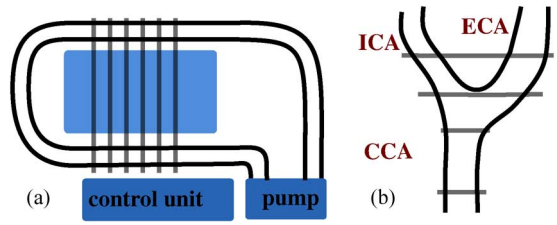

Fig. 8. Setup and imaging planes for (a) the phantom experiments and (b) the *in vivo* carotid study.

TABLE I
Quantitative Evaluation of the Phantom Data

	$\mathbf{D_{io}}$ [%]	$\mathbf{D_{si}}$ [%]	$\mathbf{D_{so}}$ [%]
Reference	2.72± 0.10	-0.73± -0.16	-1.16±0.10
MuFloCoS	3.31±0.07	2.45±0.73	2.23± 0.46

retrospectively and the undersampled data was reconstructed using our proposed MuFloCoS method. Table I illustrates the deviation results for the reference reconstruction and for MuFloCoS in percent, which are all below 4%.

B. In Vivo Study

4-D PCI data was acquired on a clinical 3T MR scanner (MAGNETOM Skyra, Siemens Healthcare, Erlangen, Germany) from 18 healthy volunteers (18–72 years) using an ECG-triggered PC sequence. The region of interest (ROI) was chosen as the region around the carotid artery bifurcation. Up to 16 transverse slices were acquired, starting from the common carotid artery (CCA) 40 mm below the bifurcation up to the internal and external carotid artery approximately 20 mm above the bifurcation. This setup is illustrated in Fig. 8(b). Imaging parameters were $\mathrm{TE/TR} = 3.5/6.22$ ms, temporal resolution 49.76 ms, flip angle 20°, FOV 200 mm × 200 mm, slice thickness 2–4 mm and imaging matrix 256 × 256, in-plane resolution of 0.78^2 mm^2. The velocity sensitivity range (ν) and phases were individually optimized. Between eleven and 20 temporal phases were acquired and the ν was chosen between 60 and 100 cm/s. The FOV was adapted if required. The fully sampled data sets were used to have a reliable reference especially for the physiological values.

Three experiments with different goals were performed with the *in vivo* study data.

Experiment I: Quantitative and physiological evaluation.

Quantitative flow parameters obtained with the proposed reconstruction algorithm are compared to previously reported literature values and to the results of different state-of-the-art iterative algorithms to ensure the validity of the proposed method for enhanced image quality and quantification purposes. Seven reconstruction were therefore performed: the fully sampled data set was reconstructed using the Sum-of-Squares technique to obtain a **Reference**. The remaining six reconstructions were performed using an acceleration factor of 9.0 for different iterative techniques. Thereby, the same coil profiles and the same formulation of the data fidelity term in (15) was used. The algorithms thus varied in the choice of the regularization, the same sampling was employed for all. All emerging optimization problems were solved using the same lBFGS method which has been

shown to be very stable and especially suited for large optimization problems as the present. The number of iterations conducted for each algorithm was determined based on the relative data fidelity term (7) reduction, calculated as

$$\epsilon^i_{DF} = \frac{\left|D(\mathbf{x}^{i-1}) - D(\mathbf{x}^i)\right|}{D(\mathbf{x}^1)}. \tag{22}$$

This resulted in $N_i = 15$ for ISENSE, $N_i = 12$ for $\mathbf{CS}_{\mathrm{wt}}$, $N_i = 12$ for $\mathbf{CS}_{\mathrm{ktFT}}$, $N_i = 9$ for $\mathbf{CS}_{\mathrm{ktPCA}}$, $N_i = 9$ for MDFCS and $N_i = 10$ for MuFloCoS.

- Iterative SENSE algorithm **ISENSE** without regularization, corresponding to $\lambda_{\mathrm{tmw}} = 0$ in (15).
- Regularized state-of-the art L_1 Compressed Sensing algorithm $\mathbf{CS}_{\mathrm{wt}}$ using the Daubechies 4 Wavelet transform and Total Variation with corner rounding parameter $\tau = 10^{-4}$.
- The kt-SPARSE SENSE algorithm as previously proposed [23] using temporal Fourier transform $\mathbf{CS}_{\mathrm{ktFT}}$ and using PCA [36] $\mathbf{CS}_{\mathrm{ktPCA}}$. The implementation followed the original implementation provided by the authors in terms of objective function and gradients.
- The previously proposed **MDFCS** algorithm [30]. A box function instead of the Gaussian weighting is used and the vessel mask is obtained only based on the dynamic images.
- The proposed **MuFloCoS** algorithm with $\lambda_{\mathrm{tmw}} = 0.004$.

The sparsity weights for $\mathbf{CS}_{\mathrm{wt}}$,$\mathbf{CS}_{\mathrm{ktFT}}$, and $\mathbf{CS}_{\mathrm{ktPCA}}$ were optimized individually for each technique regarding NRMSE over the parameter space $\lambda_{\mathrm{t}}/\lambda_{\mathrm{w}}/\lambda_{\mathrm{f}} \in [10^{-5}, 10^{-1}]$. The resulting values $\lambda_{\mathrm{t}} = 0.00005$ and $\lambda_{\mathrm{w}} = 0.00001$ for $\mathbf{CS}_{\mathrm{wt}}$, $\lambda_{\mathrm{f}} = 0.00002$ and $\lambda_{\mathrm{w}} = 0.00001$ for $\mathbf{CS}_{\mathrm{ktFT}}$ $\lambda_{pca} = 0.5$ and $\lambda_{\mathrm{w}} = 0.00001$ for $\mathbf{CS}_{\mathrm{ktPCA}}$ were used for all data sets.

Experiment II: Comparison against state-of-the art in CS for carotid PCI.

The aim of this experiment is the comparison of MuFloCoS against the only known further state-of-the-art algorithm proposed for the same application, *in vivo* imaging of the carotid arteries, the method by Tao *et al.* [28]. The key algorithmic elements were as follows.

- R: A pattern which is fully sampled in the central region and randomly under sampled in the periphery. The same percentage of central lines as in the study by Tao *et al.* (20/192) were used for the present data sets (26/256). The pattern was not varied over encodings but includes random variations over time.
- $\mathrm{L_1yf}$: $\mathrm{L_1}$ minimization in the yf-space for each encoding separately was proposed as regularization by Tao *et al.*

Different reconstructions, evaluating these components against the corresponding MuFloCoS parts, the I-VT sampling and the TMW regularization were evaluated. First, the proposed method was evaluated as proposed in the original paper combining a random pattern with the $\mathrm{L_1yf}$ minimization (TAO 3) and with the same acceleration of 3 and regularization but using the I-VT pattern ($\mathrm{I-VT+L_1yf}$ 3). Then, three reconstruction were performed with an acceleration factor of 9: The method by Tao *et al.* (TAO 9), the novel I-VT sampling combined with the $\mathrm{L_1yf}$ regularization ($\mathrm{I-VT+L_1yf}$ 9) and finally the proposed MuFloCoS method. To ensure fair comparison, the weights were optimized regarding NRMSE for each of these experiments, but kept fixed over all data sets.

Experiment III: Parameter and robustness.

The influence, stability and robustness of different algorithmic aspects and parameter choices are evaluated based on quantitative image measures and reconstruction parameters. For Experiment III, three elements were investigated: The regularization weight λ_{tmw}, the sampling strategy and the use of the shared coil profile calculation. The parameter λ_{tmw} was varied between 0.0005 and 0.0125, the sampling pattern was chosen fixed for all phases and temporal phases or interleaved and permuted with regular permutations with length 1 or interleaved and permuted as proposed by the I-VT sampling strategy of MuFloCoS. The basis pattern parameters $\mathbf{o_c}$, $\mathbf{d}_{\mathrm{c}}$, a, and b were chosen identical for both. Furthermore, the influence of coil sensitivity calculation was evaluated by using either the shared version or by acquiring an external reference scan, both resulting in a total of 16 used reference lines. Feasible acceleration factors for this application are determined, the used acceleration factor was therefore varied between 3, 6, 9, 12, and 15. The reconstructions were performed with fixed $\lambda_{\mathrm{tmw}} = 0.004$.

1) Evaluation Strategy: The reconstructed volumes $\mathbf{x}$ are used to calculate the angiographic images $\mathbf{a}$ and the phase contrast images $\mathbf{p}$. For the derivation of flow parameters, the 3-D velocity fields $\mathbf{V}$ and the vessel borders Λ for the CCA, ICA, and ECA are required. The borders are obtained using an interactive up-sampling and segmentation tool. For the quantitative image evaluation, the normalized root mean square error NRMSE and the structural similarity measure SSIM [37] offer an objective comparison between the reconstruction result $\mathbf{t} \in \mathbb{C}^N$ and reference volume $\mathbf{r} \in \mathbb{C}^N$. Thereby $\mu(\mathbf{x})$ and $\sigma(\mathbf{x})$ are the mean and respectively the variance over $\mathbf{x}$. Furthermore, to assess the image quality, the angiography specific contrast-to-noise-ratio between vessel and tissue CNRVT was used. Therefore, regions-of-interest (ROI) were chosen in the vessel $\mathbf{t}_v$ and the tissue $\mathbf{t}_t$.

Evaluated flow parameters include the volumetric flow rate $Q_v(t)$, the peak velocity $V_p(t)$ and the mean velocity $V_m(t)$. They were measured in the 2-D slices and in three selected vessel cross sections as illustrated in Fig. 8(b). The temporal normalized root mean square error is calculated for a dynamic parameter $\mathrm{TN}(P, \mathbf{r}, \mathbf{t})$, measured with a reference method $P_{\mathbf{r}} \in \mathbf{R}^N_t$ and with a test method $P_{\mathbf{t}} \in \mathbf{R}^N_t$. These values are computed as

$$\mathbf{NRMSE}(\mathbf{r}, \mathbf{t}) = \frac{1}{N}\|\mathbf{r} - \mathbf{t}\|_{L_2}$$

$$\mathbf{TN}(P, \mathbf{r}, \mathbf{t}) = \frac{1}{N_t}\left\|\frac{P_{\mathbf{r}} - P_{\mathbf{t}}}{P_{\mathbf{r}}}\right\|_{L_2}$$

$$\mathbf{CNRVT}(\mathbf{t}_v, \mathbf{t}_t) = \frac{\mu(\mathbf{t}_v) - \mu(\mathbf{t}_t)}{\sqrt{0.5\left(\sigma(\mathbf{t}_v)^2 + \sigma(\mathbf{t}_t)^2\right)}}$$

and

$$\mathbf{SSIM}(\mathbf{r}, \mathbf{t}) = \frac{2\mu(\mathbf{r})\mu(\mathbf{t}) + c_1}{\mu(\mathbf{T})^2 + \mu(\mathbf{r})^2 + c_1} + \frac{\sigma\sigma(\mathbf{t}, \mathbf{r}) + c_2}{\sigma(\mathbf{r})^2 + \sigma(\mathbf{t})^2 + c_2}.$$

The deviation is calculated for the volumetric flow $Q_v(t)$ and for the peak velocity $V_p(t)$. Those results are illustrated with Bland-Altman diagrams for graphical illustration of the TNRMSE for

TABLE II
QUANTITATIVE IMAGE AND PHYSIOLOGY-BASED EVALUATION FOR THE *IN VIVO* STUDY COMPARING MUFLOCOS TO THE REFERENCE AND FURTHER ITERATIVE METHODS

	NRMSE	SSIM	CNRVT
Ref.	0.0 ± 0.0	1.0 ± 0.0	6.366 ± 1.643
ISENSE	0.118 ± 0.033	0.735 ± 0.146	4.117 ± 1.077
CS$_{\mathrm{wt}}$	0.070 ± 0.022	0.861 ± 0.073	5.441 ± 1.235
CS$_{\mathrm{ktFT}}$	0.069 ± 0.018	0.870 ± 0.083	5.261 ± 1.230
CS$_{\mathrm{ktPCA}}$	0.108 ± 0.031	0.747 ± 0.140	4.759 ± 1.151
MDFCS	0.076 ± 0.021	0.841 ± 0.098	5.620 ± 1.201
MuFloCoS	0.058 ± 0.015	0.893 ± 0.067	6.293 ± 1.217
	TN(Q_v)	**TN**(V_p)	
Reference	0.0 ± 0.0	0.0 ± 0.0	
ISENSE	0.167 ± 0.075	0.324 ± 0.155	
CS$_{\mathrm{wt}}$	0.080 ± 0.034	0.158 ± 0.029	
CS$_{\mathrm{ktFT}}$	0.106 ± 0.062	0.139 ± 0.090	
CS$_{\mathrm{ktPCA}}$	0.089 ± 0.033	0.164 ± 0.056	
MDFCS	0.113 ± 0.062	0.117 ± 0.061	
MuFloCoS	0.106 ± 0.052	0.076 ± 0.031	

all data sets and for each combination between MuFloCoS and state-of-the-art methods. The results are ordered by the absolute values for the volumetric flow and the peak velocity of the data sets. This illustration aids to identify any systematic errors or outliers.

2) Results for Experiment I: Quantitative and Physiological Evaluation: The quantitative results for the image based measures of the study with 18 data sets are shown in Table II for MuFloCoS and the five comparison methods. The NRMSE of MuFloCoS is significantly reduced compared to the iterative SENSE reconstruction and all further considered methods. Statistically, the NRMSE has been improved by 50.85 compared to ISENSE, by 15.94 in comparison to $\mathbf{CS}_{\mathrm{ktFT}}$ and by 17.14 compared to $\mathbf{CS}_{\mathrm{wt}}$. The same is valuable for the structural similarity SSIM, which was improved by 3.72 compared to the best comparison method $\mathbf{CS}_{\mathrm{wt}}$. The contrast-to-noise ratio between the vessel and the background could be improved for all data sets, in the mean by at least 16.5 and up to 41.2. Table II shows the mean deviation from the physiological parameters for each reconstruction technique. One data set (P16) was excluded from the calculation of physiological parameters, as the overall image quality even for the reference did not allow stable evaluation. A significant improvement was achieved for the peak velocity with 45.32% lower TN compared to $\mathbf{CS}_{\mathrm{ktFT}}$ and 53.04% lower TN compared to MDFCS. While $\mathbf{CS}_{\mathrm{ktPCA}}$ performed better regarding the volumetric flow by 16.82%, MuFloCoS was significantly better in the peak flow velocity measurements with an improvement of 53.7%. Fig. 9 illustrates two representative results for peak systole. Representative time curves are shown in Fig. 10, displaying the volumetric flow in the first row, the mean velocity in the second row and the peak velocity in the last row for all reconstruction results. The curves of the reference and MuFloCoS are very similar, while the other methods except $\mathbf{CS}_{\mathrm{wt}}$ tend to overestimate volumetric flow and mean velocity in both cases. The most significant difference is visible in the peak velocity plots, which is heavily disturbed for comparison methods but well preserved for MuFloCoS. Especially the $\mathbf{CS}_{\mathrm{wt}}$ method, which produced a lower error in volumetric flow significantly underestimated the peak velocity. The Bland-Altman diagrams for the best comparison methods $\mathbf{CS}_{\mathrm{wt}}$, $\mathbf{CS}_{\mathrm{ktFT}}$, and $\mathbf{CS}_{\mathrm{ktPCA}}$ are given in Figs. 11. No outlier

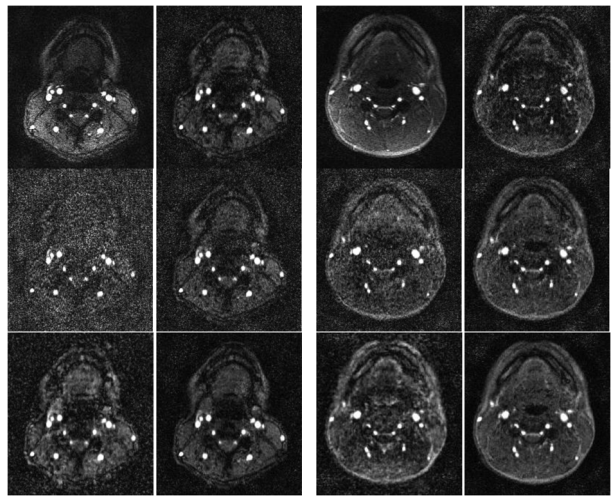

Fig. 9. Magnitude reconstruction results for the through-plane encoding for volunteer P2 and P7 at peak systole. Shown for both in the top row: Reference, $\mathbf{CS}_{\mathrm{ktFT}}$, in the middle row: ISENSE, MDFCS and in the bottom row: $\mathbf{CS}_{\mathrm{wt}}$, MuFloCoS.

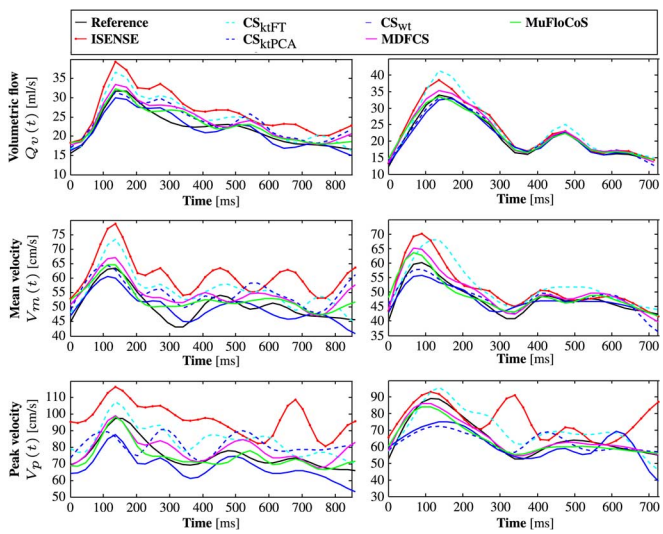

Fig. 10. Volumetric flow, mean velocity profile, and peak velocity profiles illustrated for volunteers P6 and P7.

or systematic bias is visible in the MuFloCoS result, whereas the values for the other methods are spread for both volumetric flow and peak velocity. Fig. 12 illustrates the 3-D result for peak systole and early diastole at three selected locations as depicted in Fig. 8(b).

3) Results for Experiment II: Comparison Against Carotid PCI State of the Art: With the original method proposed by Tao *et al.* [28], very good results were achieved for an acceleration factor of 3, with a SSIM of 0.934 ± 0.038, a NRMSE of 0.064 ± 0.023 and a TNRMSE of the volumetric flow of 0.123 ± 0.104 for the random pattern. The results using the same regularization but the proposed I-VT sampling further increase image quality and the accuracy of the physiological values with a NRMSE of 0.042 ± 0.011 and TNRMSE of the peak velocity of 0.161 ± 0.060. For the higher factor of 9, however, the proposed MuFloCoS algorithm outperforms this method, particularly with

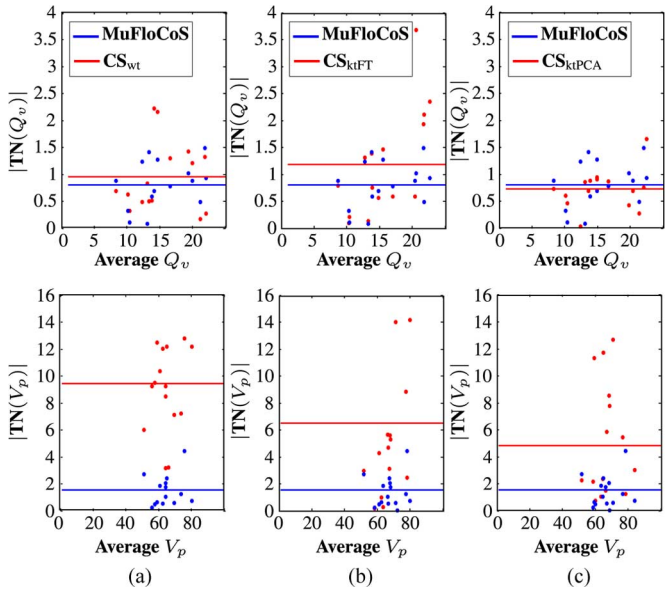

Fig. 11. Bland-Altman diagram for volumetric flow and peak velocity for the *in vivo* study for MuFloCoS and (a) $\mathbf{CS}_{\mathrm{wt}}$, (c) $\mathbf{CS}_{\mathrm{ktFT}}$, and (c) $\mathbf{CS}_{\mathrm{ktPCA}}$.

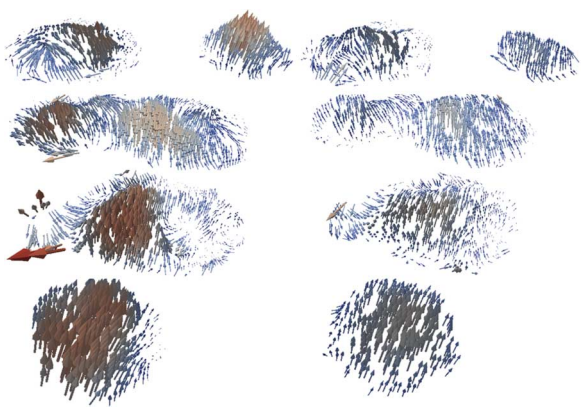

Fig. 12. 3-D velocity vector field from the left carotid bifurcation region illustrated with 3-D vectors at four different locations for peak systole and early diastole.

TABLE III
QUANTITATIVE IMAGE-BASED EVALUATION FOR THE *IN VIVO* STUDY COMPARING MUFLOCOS AGAINST THE RESULTS OF CAROTID PCI STATE-OF-THE-ART

	NRMSE	SSIM	CNRVT
Ref.	0.0 ± 0.0	1.0 ± 0.0	6.366 ± 1.643
TAO 3	0.064 ± 0.023	0.934 ± 0.038	6.576 ± 1.370
TAO 9	0.088 ± 0.026	0.931 ± 0.043	6.504 ± 1.007
I-VT+L$_1$yf 3	0.042 ± 0.011	0.950 ± 0.031	6.559 ± 1.33
I-VT+L$_1$yf 9	0.065 ± 0.025	0.876 ± 0.068	5.478 ± 1.078
MuFloCoS 9	0.058 ± 0.015	0.893 ± 0.067	6.293 ± 1.217
	CNRVB	**TN**(Q_v)	**TN**(V_p)
Ref.	8.703 ± 1.791	0.0 ± 0.0	0.0 ± 0.0
TAO 3	8.481 ± 1.853	0.123 ± 0.104	0.176 ± 0.097
TAO 9	9.510 ± 1.749	0.171 ± 0.106	0.242 ± 0.088
I-VT+L$_1$yf 3	8.297 ± 1.649	0.085 ± 0.037	0.161 ± 0.060
I-VT+L$_1$yf 9	6.969 ± 1.263	0.119 ± 0.087	0.173 ± 0.079
MuFloCoS 9	8.170 ± 1.522	0.106 ± 0.052	0.076 ± 0.031

respect to the TNRMSE of the physiological values and the NRMSE. However, the method of Tao *et al.* shows some advantages regarding the SSIM value and the CNR. Comparing

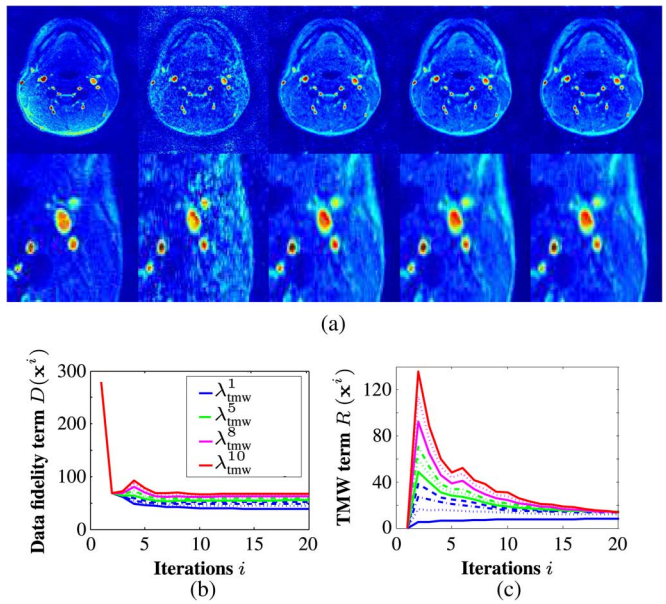

Fig. 13. Image and reconstruction parameter results for a representative volunteer using different λ_{tmw}. (a) Image results and zooms to the right ICA for, from left to right, the reference and MuFloCoS with $\lambda_{\mathrm{tmw}} = [0.0005, 0.0045, 0.0085, 0.0125]$. (b), (c) Evolution of the data fidelity term (b) and TMW term (c) is depicted for 20 iteration steps.

TABLE IV
QUANTITATIVE IMAGE BASED EVALUATION FOR DIFFERENT MUFLOCOS VARIANTS

	Reference	MuFloCoS	Static pattern	Ext. coil maps
NRMSE	0.0	5.53± 0.009	5.90± 0.013	5.79± 0.006
SSIM	1.0	0.84± 0.01	0.84± 0.01	0.84± 0.01
CNRVB	7.73± 3.21	7.47± 1.37	6.70± 2.28	7.37± 1.86
TN(Q_v)	0.0	7.10± 0.01	8.87± 0.15	5.66± 0.01
TN(V_p)	0.0	5.54± 0.01	8.10± 0.20	5.44± 0.03

the results using the L$_1$yt regularization in combination with either the random or the I-VT pattern, the I-VT pattern delivers more accurate flow results and better NRMSE, but lower SSIM and CNR.

4) Results for Experiment III: Robustness and Acceleration: Image results for different λ_{tmw} values are shown in Fig. 13(a) with a zoom to the right carotid artery. The data fidelity term as well as the TMW regularization term for selected choices of λ_{tmw} are illustrated in Fig. 13(b) and (c). This reconstruction resulted in the values illustrated in Table IV. The respective images for $s = 4$ for early diastole ($t_3 = 136$ ms) and difference images to the complete MuFloCoS method are shown for MnP and MnC in Fig. 14 along with the corresponding difference images to the normal MuFloCoS in the lower row. Volumetric flow and mean velocity are illustrated in Fig. 15. Reconstruction specific parameters including the data fidelity term and the regularization term over time are illustrated in the lower row of Fig. 15. Both the data fidelity and the L$_1$ norm show a similar behavior for M and MnC, but higher values for the variant without the interleaved and shifted pattern (MnP). Results of varying acceleration factors of 3, 6, 9, 12, and 15 and fixed λ_{tmw} can be seen for $s = 4$ for the entire image and a zoom in Fig. 16(a). The corresponding curves for volumetric flow are illustrated in Fig. 16(b), the peak velocity in Fig. 16(c).

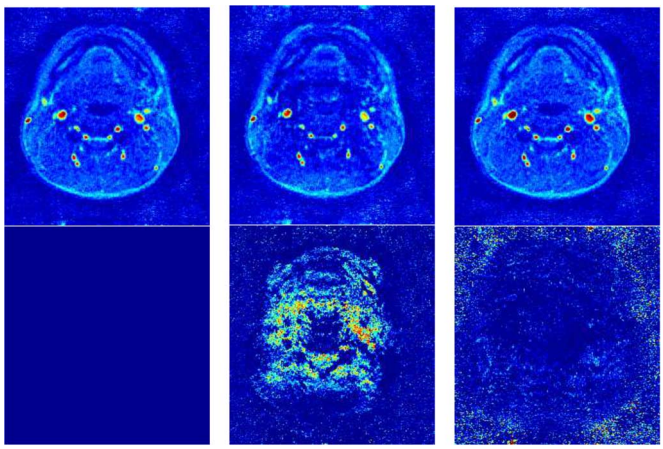

Fig. 14. Image results for the through-plane encoding comparing the reference and MuFloCoS (a) with the I-VT pattern and the shared coil profiles, (b) without the I-VT pattern, and (c) with external coil profiles. Lower row illustrates the difference to MuFloCoS scaled by a factor of 10.

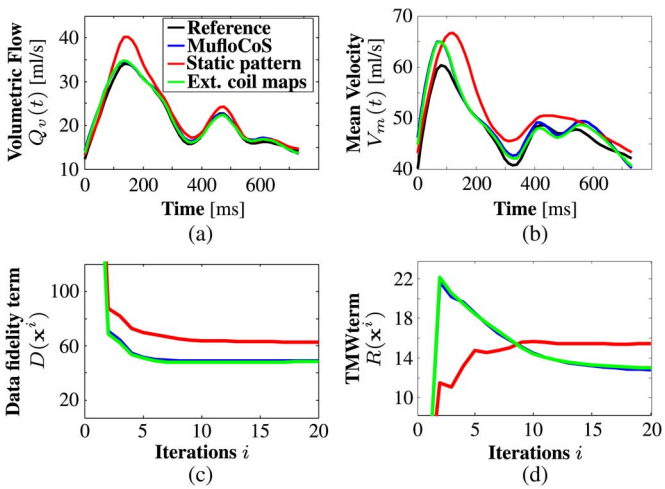

Fig. 15. Physiological parameters (a), (b) and reconstruction results (c), (d) for MuFloCoS with the I-VT pattern and the shared coil profiles, without the I-VT pattern and with external coil profiles. Volumetric flow $Q_v(t)$ and mean velocity $V_m(t)$ are shown. Evolution of the data fidelity term and the evolution of the TMW-L_1 term are depicted for 20 iteration steps.

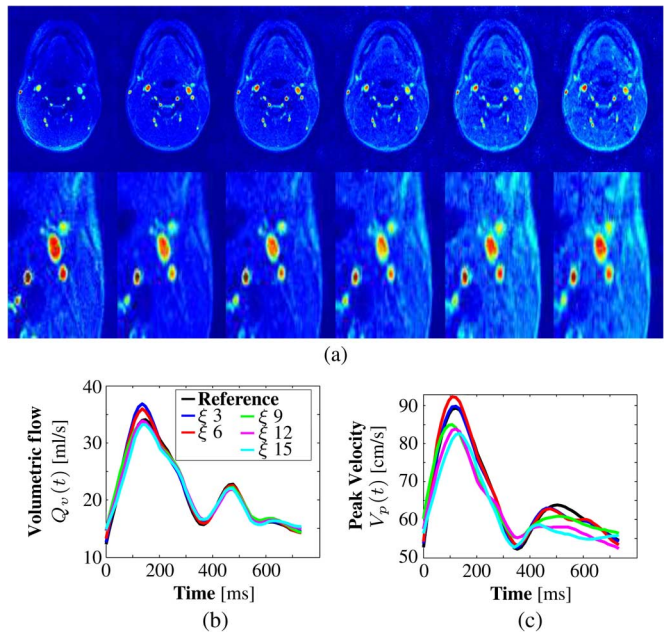

Fig. 16. Image results and physiological parameters for a representative volunteer for different acceleration factors $\xi = 3, \xi = 6, \xi = 9, \xi = 12$, and $\xi = 15$. (a) Image results from the through-plane encoding. (b) Volumetric flow $Q_v(t)$ and (c) peak velocity $V_p(t)$.

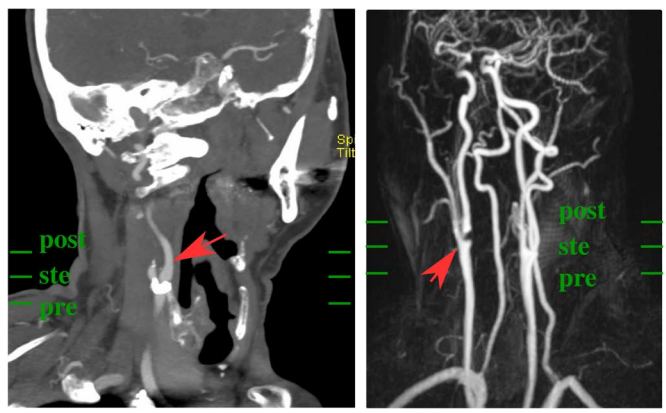

Fig. 17. Diagnostic data from two patients with severe ICA stenosis. Patient 1: (a) coronar MIP highlighting the plaque around the right carotid bifurcation. Patient 2: (b) DCE-MRI indicating the severe stenosis of the right ICA. Locations of the chosen PCI slices are highlighted in green.

C. Patient Cases

Two patients m/72y, m/63y, diagnosed with stenosis in the ICA, were examined on a clinical 3T MR scanner (MAGNETOM Verio, Siemens AG Healthcare Sector, Erlangen, Germany) using an ECG-triggered PC MRI sequence. Patient 1 was diagnosed with a high-grade stenosis of the right ICA (NASCET 80%) and a low-grade stenosis of the left ICA on CTA and DUS as indicated by red arrows on the coronar CTA maximum-intensity projections in Fig. 17. For patient 2, DCE-MRI revealed the unilateral high-grade stenosis of the right ICA, as shown in Fig. 17. Both patients were scheduled for an endartectomy. Axial slices at three locations pre- and post the respective stenosis, "pre," "ste," and "post," were acquired with TE/TR 3.96/3.25(3.96 ms/6.51 for Patient 2) ms, temporal resolution 26.04 ms. flip angle 20°, FOV 200 × 200 mm^2, slice thickness 4 mm, imaging matrix 224 × 224, and in-plane resolution of 0.89^2 mm^2, to evaluate the flow and velocity profiles. The venc was chosen as $\nu = 180\ \mathrm{cm/s}$ (150 cm/s) and the number of temporal phases as $N_t = 26$ ($N_t = 15$).

1) Results: The under sampled data was reconstructed with MuFloCoS and evaluated with a special focus on the pathology detection by analyzing the peak velocities in the CCA and ICA at three positions in the CCA, in close proximity to the stenosis and post-stenotic in the ICA. For patient 1, the corresponding peak velocity plots are illustrated in Fig. 18(a). A clear difference is visible between the velocities in the pre-stenotic CCA and after the stenosis in the ICA. Especially on the right side, where the high-degree stenosis has been diagnosed, a sharp increase in peak-velocity is observable, which correlates well with the reduced lumen at this position. The difference between the high-grade stenosis on the right side to the low-grade stenosis

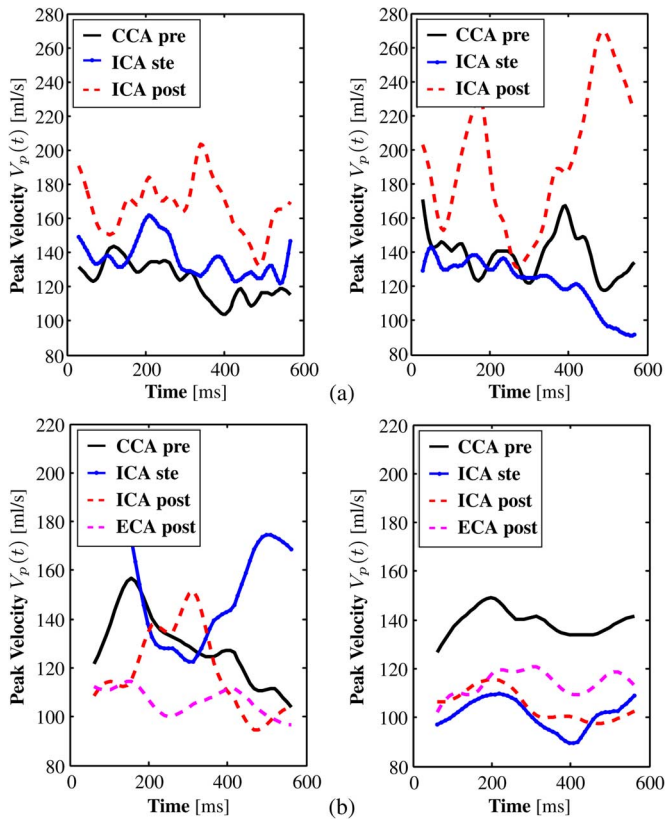

Fig. 18. Peak velocity profiles for patient 1 and 2 from the PCI scan, accelerated with factor $\xi = 9.0$ and reconstructed using MuFloCoS.

on the left side is well visible in the difference of the peak velocities. The results for patient 2 in Fig. 18(b) indicate well the unilateral stenosis diagnosed with DCE-MRI. The stenotic profile in the ICA is corrupted by aliasing due to the high velocites. No correction was applied to this.

V. Discussion

Iterative reconstruction with the proposed MuFloCoS method was successful for all phantom and *in vivo* experiments and produced comparable consistent results. The high noise level both in the background and the tissue of the image reconstructed with iterative SENSE was significantly reduced with the iterative methods. While they all managed to recover the image structures, the quality of the images as well as the accuracy of the physiological parameters are measurable better for MuFloCoS. The image quality allowed in summary good visualization of the anatomy and corresponds to that of the fully sampled reference image.

A. Quantitative Evaluation

In the phantom experiment, all inter- and intra-slice deviations were under 4%, which illustrates the capability of MuFloCoS to preserve the flow values over the entire dataset. Concerning the *in vivo* data, the evaluation of the flow parameters showed good preservation of flow parameters and had a significantly reduced deviation compared to the further methods in both the phantom experiment and the volunteer study (see Table I, II). With MuFloCoS, the volumetric flow $Q_v(t)$, the mean velocity $V_m(t)$ and the peak velocity $V_p(t)$ over time (Fig. 10) in the CCA were in good agreement with the corresponding values obtained with the fully sampled directly reconstructed data sets. A comparison to further state of the art methods showed improvements in NRMSE, SSIM, and particularly in the peak velocity, which is an important diagnostic value in the classification of stenosis. This result indicates that both temporal and spatial resolution are well preserved. Volumetric flow and mean velocity corresponded well to values for the volumetric flow rate as previously reported by Long *et al.* [38], and for the mean velocity obtained by Ringgaard *et al.* [39]. The patient cases and the respective peak velocity profiles shown in 18 confirmed the CT and DCE-MRA findings and even allowed differentiating between high- and low-grade stenosis.

The results compared to the PCA regularization as proposed by Kim *et al.* [23] revealed a slight advantage for this regularization for the evaluation of the volumetric flow, which shows, that a combination of the global PCA method with the proposed temporal masked and weighted MuFloCoS regularization is of huge interest. The method as shown in [23] was a two step method, starting with Fourier Transform and than switching to PCA, which was not done in this analysis to make it comparable to the further methods. Including the proposed MuFloCoS algorithm for the first step instead of the temporal Fourier transform, and adding the temporal PCA at a later stage could further add value. The improvement compared to MDFCS shows the positive influence of combining static and dynamic anatomical images and of the Gaussian weighting. The comparison against state-of-the art for CS methods applied to carotid PCI indicated the improvements achieved with MuFloCoS regarding both image- and physiology-based measures, particularly in for higher acceleration factors.

For carotid PCI accelerated by factor 9.0, the comparison with the method by Tao *et al.* revealed significant advantages for the novel MuFloCoS method, particularly regarding the physiological values. The proposed method by Tao *et al.* showed, however, good results for the SSIM and the CNR. Regarding the desired hemodynamic information obtained from PCI acquisitions, the accuracy of the physiological values is of major interest. Further investigation could include a combination of both regularization terms in the objective function.

B. Evaluation of I-VT, shared coil profiles and TMW

The benefits of the masked temporal regularization and the I-VT pattern to exploit the inherent data correlation both in velocity encoding and temporal direction become evident with the results of their respective influence. The shared coil profile calculation led to a very slight change in the results for NRMSE from 5.53 to 5.79 while it contributed to the final acceleration in substantial amount by allowing real undersampling by factor four in the central k-space. Its influence, illustrated in Fig. 14(b), was barely visible in the difference image where the main deviations occur outside the object. The influence of the interleaved and shifted pattern was substantially higher, as shown in Table IV and in image 14(c). The L_1 norm plot in Fig. 15 on the left illustrates that the higher similarity at the beginning due to the same sampling, expressed through low L_1 difference values, increased with iterations and converged at higher values

$$u_{\kappa}^{t,s} = \begin{cases} 1, & \text{for } \kappa_y = \kappa_{my} - \left\lfloor \frac{N_{\kappa_{cy}}}{2} \right\rfloor + o_{cy}\left(j(t,s)\right) + id_{cy} \\ & \text{where } i \in \mathbb{N} \text{ such that } (\kappa_x, \kappa_y) \in \mathcal{C} \\ 0, & \text{else.} \end{cases} \tag{23}$$

$$u_{\kappa}^{t,s} = \begin{cases} 1, & \text{for } \kappa_y = \kappa_{my} - \left\lfloor \frac{N_{\kappa_{cy}}}{2} \right\rfloor - \left(o_{cy}\left(j(t,s)\right) + s\left(i,(a,b)\right)\right) \\ & \text{where } i \in \mathbb{N} \text{ such that } (\kappa_x, \kappa_y) \in \mathcal{P} \\ 1, & \text{for } \kappa_y = \kappa_{my} + \left\lfloor \frac{N_{\kappa_{cy}}}{2} \right\rfloor + \left(o_{cy}\left(j(t,s)\right) + s\left(i,(a,b)\right)\right) \\ & \text{where } i \in \mathbb{N} \text{ such that } (\kappa_x, \kappa_y) \in \mathcal{P} \\ 0, & \text{otherwise.} \end{cases} \tag{24}$$

than the I-VT pattern variant. This can be explained by the property of the I-VT pattern to allow a better minimization for the whole objective function (15) including data fidelity term and regularization term. The NRMSE decreased from 5.90 to 5.53 compared to the shifted and interleaved pattern.

Experiment III illustrated furthermore that the proposed TMW-L_1 regularization offers a very stable regularization option. Different choices of the weighting factor λ_{tmw} led to comparable results both in terms of visual impression and in the physiological parameter estimation. Fig. 13(a) and (b) illustrated even a convergence for both the data fidelity term, as well as for the TMW-L_1 term independent of λ_{tmw}. For λ_{tmw} in the range of [0.0015, 0.0125], the term converged to the same value after 20 iterations. No critical bound was obtained, the changes with growing λ_{tmw} are smooth in Fig. 13(a). All reconstructions for the 18 volunteers were performed with a fixed $\lambda_{\text{tmw}} = 0.0040$ and produced comparable results, the parameter can therefore be assumed to be robust in a wide range and stable over different data sets.

Experiment II illustrated furthermore the acceleration capacities of MuFloCoS. Even for high factors, such as 15, resulting in using only around 6.7% of the data, good physiological results could be achieved. This acceleration is significantly higher than feasible with currently clinically used methods, which can achieve an acceleration of 2–4 (25%–50% of the data) in this application. The performed study had the limitation that the reference values are calculated based on the fully sampled PC MRI scans. This provided a reliable reference for the physiological values. Further prospective under sampled studies need to be done in the future. A further extension could be direct comparison with a different modality such as a flow meter or DUS.

VI. Conclusion

Acceleration factors of $\xi = 9.0$ in volunteers have been successfully applied to PCI, leading to a significant speed up of the acquisition. The acquisition time for good temporal and spatial resolution in the carotid artery region can be significantly reduced. For the concrete example of the patient data acquisition using three three-directional 2-D slices pre- and post-stenosis in the CCA and ICA, the acquisition time could be reduced from 8 min 24 s to 56 s. This significant reduction can be an important step in the clinical acceptance of this technique. This saved time could also be invested in a higher spatial and/or temporal resolution allowing to visualize especially pathological hemodynamic situations with better accuracy. The proposed method is not limited to the introduced masked and weighted temporal regularization, but is easily expendable to different regularizers such as TV, Wavelet or more PCI specific constraints as divergence free flow fields or phase constraint. Only intrinsic properties of the 4-D PCI acquisition were exploited which makes the proposed method ideally suited to be applied to different body regions imaged with PCI.

TABLE V

N	Number of image space voxels ($N = N_x N_y N_z$)
N_k	Number of k-space voxels ($N_k = N_{k_x} N_{k_y} N_{k_z}$)
N_c / N_t /N_s	Number of channels / time steps / encodings
N_p	Problem size ($N_p = N_t N_s$)
N_i	Number of iterations
ι / κ	Image /k-space voxel index
$\mathbf{x}$	Image space vector for all time steps and encodings
$\mathbf{x}^{t,s}$	Image space vector
$\mathbf{m}_{\gamma}^{t,s}$ / $\mathbf{m}^{t,s}$	k-space vector for coil γ / all coils
$\mathbf{u}_{\boldsymbol{\kappa}}^{t,s}$	Sampling pattern
$N_{\kappa_{cy}} \times N_{\kappa_{cz}}$	k-space center size
a, b	Parameter for the decreasing density sampling
$\mathbf{d_c}, \mathbf{o_c}, j(t,s)$	Parameter for the k-space center sampling
$D(\mathbf{x})$ / $R(\mathbf{x})$	Data fidelity / regularization term
λ_{tmw}	Weighting parameter of the regularization
$\mathcal{S}$	Sum-of-Squares reconstruction matrix
$\mathbf{E}$	Iterative SENSE reconstruction matrix
ι_V / ι_M / ι_M	Index set of the entire / flow affected /static volume
$\bar{\mathbf{a}}$/$\check{\mathbf{a}}$	Static / dynamic anatomical image
$\bar{\mathbf{b}}$ / $\check{\mathbf{b}}$	Static /dynamic binary mask
l	Threshold parameter used in the mask thresholding
$\mathbf{b}^t$	Vessel mask for time step t
$\mathbf{M}$	Vessel mask matrix
$\mathbf{W}$	Weighting matrix
$\nabla_t \mathbf{x}$	Temporal difference
$w(t, t_j)$	Weighting function
σ	Gaussian standard deviation
ϵ	Parameter defining the support of $w_G(t, t_j)$
$Q_v(t)$ / $V_p(t)$ /$V_m(t)$	Volumetric flow / Peak velocity /Mean velocity
D_{io} / $D_{si/o}$	Deviation between in/outflow / slices

Appendix

Annex A: Pattern Calculation

See (23) and (24) at top of the page.

Annex C: Symbol Table

See Table V.

Acknowledgment

The authors gratefully acknowledge funding of the Erlangen Graduate School in Advanced Optical Technologies (SAOT) by the German Research Foundation (DFG) in the framework of the German excellence initiative. The authors further thank the

authors of the paper [23] for providing the code for the temporal FT and PCA regularization.

REFERENCES

[1] , R. G. González, J. A. Hirsch, M. H. Lev, P. W. Schaefer, and L. H. Schwamm, Eds., *Acute Ischemic Stroke, Imaging and Intervention*, 2nd ed. New York: Springer, Oct. 2011.

[2] A. F. Stalder, M. F. Russe, A. Frydrychowicz, J. Bock, J. Hennig, and M. Markl, "Quantitative 2-D and 3-D phase contrast MRI: Optimized analysis of blood flow and vessel wall parameters," *Magn. Reson. Med.*, vol. 60, no. 5, pp. 1218–1231, Nov. 2008.

[3] N. H. J. Pijls, B. de Bruyne, K. Peels, P. H. van der Voort, H. J. R. M. Bonnier, J. Bartunek, and J. J. Koolen, "Measurement of fractional flow reserve to assess the functional severity of coronary-artery stenoses," *N. Eng. J. Med.*, vol. 334, no. 26, pp. 1703–1708, Jun. 1996.

[4] A. Harloff, T. Zech, F. Wegent, C. Strecker, C. Weiller, and M. Markl, "Comparison of blood flow velocity quantification by 4-D Flow MR imaging with ultrasound at the carotid bifurcation," *AJNR Am. J. Neuroradiol.*, vol. 34, no. 7, pp. 1407–1413, Feb. 2014.

[5] I. Marshall, S. Zhao, P. Papathanasopoulou, P. Hoskins, and Y. Xu, "MRI and CFD studies of pulsatile flow in healthy and stenosed carotid bifurcation models," *J. Biomech.*, vol. 37, no. 5, pp. 679–687, May 2004.

[6] J. Endres, T. Redel, M. Kowarschik, J. Hutter, J. Hornegger, and A. Dörfler, "Virtual angiography using CFD simulations based on patient-specific parameter optimization," in *Proc. 9th IEEE Int. Symp. Biomed. Imag.*, Barcelona, Spain, 2012, pp. 1200–1203.

[7] M. Markl, M. T. Draney, M. D. Hope, J. M. Levin, F. P. Chan, M. T. Alley, N. J. Pelc, and R. J. Herfkens, "Time-resolved 3-dimensional velocity mapping in the thoracic aorta: Visualization of 3-directional blood flow patterns in healthy volunteers and patients," *J. Comput. Assist. Tomogr.*, vol. 28, no. 4, pp. 459–468, Jul./Aug. 2004.

[8] F. Santini, S. G. Wetzel, J. Bock, M. Markl, and K. Scheffler, "Time-resolved three-dimensional (3-D) phase-contrast (PC) balanced steady-state free precession (bSSFP)," *Magn. Reson. Med.*, vol. 62, no. 4, pp. 966–974, Oct. 2009.

[9] R. Hausmann, J. S. Lewin, and G. Laub, "Phase-contrast MR angiography with reduced acquisition time: New concepts in sequence design," *J. Magn. Reson. Imag.*, vol. 1, no. 4, pp. 415–422, Jul./Aug. 1991.

[10] M. A. Griswold, P. N. Jakob, R. M. Heidemann, M. Nittka, V. Jellus, J. Wang, B. Kiefer, and A. Haase, "Generalized autocalibrating partially parallel acquisitions (GRAPPA)," *Magn. Reson. Med.*, vol. 47, pp. 1202–1210, Jun. 2002.

[11] K. P. Pruessmann, M. Weiger, M. B. Scheidegger, and P. Boesiger, "SENSE: Sensitivity encoding for fast MRI," *Magn. Reson. Med.*, vol. 42, no. 5, pp. 952–962, Nov. 1999.

[12] Z. Stankovic, J. Fink, M. Russe, M. Markl, and B. A. Jung, "On the use of K-T accelerated 4-D flow MRI in the portal system," in *Proc. 21st Annu. Meet. ISMRM*, Salt Lake City, UT, 2013, p. 4451.

[13] D. Giese, T. Schaeffter, and S. Kozerke, "Highly undersampled phase-contrast flow measurements using compartmentbased k-t principal component analysis," *Magn. Reson. Med.*, vol. 69, no. 2, pp. 434–443, Apr. 2012.

[14] J. A. Steeden, D. Atkinson, M. S. Hansen, A. M. Taylor, and V. Muthurangu, "Rapid flow assessment of congenital heart disease with high-spatiotemporal-resolution gated spiral phase-contrast MR imaging," *Radiology*, vol. 260, no. 1, pp. 79–87, Jul. 2011.

[15] M. Lustig and J. M. Pauly, "Spirit: Iterative self-consistent parallel imaging reconstruction from arbitrary k-space," *Magn. Reson. Med.*, vol. 64, no. 2, pp. 457–471, Aug. 2010.

[16] E. J. Candès and M. B. Wakin, "An introduction to compressive sampling," *IEEE Signal Process. Mag.*, vol. 25, no. 2, pp. 21–30, Mar. 2008.

[17] J. I. Jackson, C. H. Meyer, D. G. Nishimura, and A. Macovski, "Selection of a convolution function for Fourier inversion using gridding," *IEEE Trans. Med. Imag.*, vol. 10, no. 3, pp. 473–478, Sep. 1991.

[18] M. Doneva, H. Eggers, and P. Börnert, "CS-SENSE or denoised sense: The influence of irregular sampling in l1 regularized sense reconstruction," in *Proc. 20th Annu. Meet. ISMRM*, Melbourne, Australia, May 2012, p. 2240.

[19] J. Yellott, "Spectral consequences of photoreceptor sampling in the rhesus retina," *Science*, vol. 221, no. 4608, pp. 382–385, Jul. 1983.

[20] Y. Kwak, S. Nam, K. V. Kissinger, B. Goddu, L. Goepfert, W. Manning, V. Tarokh, and R. Nezafat, "Accelerated phase contrast imaging using compressed sensing with complex difference sparsity," *J. Cardiovasc. Magn. Reson.*, vol. 14, p. W24, Feb. 2012.

[21] J. Busch, D. Giese, L. Wissmann, and S. Kozerke, "Divergence-free reconstruction for accelerated 3-D phasecontrast flow measurements," *J. Cardiovasc. Magn. Reson.*, vol. 14, p. W38, Feb. 2012.

[22] F. Zhao, D. Noll, J. Nielsen, and F. Fessler, "Separate magnitude and phase regularization via compressed sensing," *IEEE Trans. Med. Imag.*, vol. 31, no. 9, pp. 1713–1723, Sep. 2012.

[23] D. Kim, H. A. Dyvorne, R. Otazo, L. Feng, D. K. Sodickson, and V. S. Lee, "Accelerated phase-contrast cine MRI using k-t SPARSE-SENSE," *Magn. Reson. Med.*, vol. 67, pp. 1054–1064, Apr. 2012.

[24] J. V. Velikina, K. M. Johnson, W. F. Block, and A. A. Samsonov, "Design of temporally constrained compressed sensing methods for accelerated dynamic MRI," in *Proc. Joint Annu. Meet. ISMRM—ESMRMB*, Stockholm, Sweden, May 2010, p. 4865.

[25] J. P. Hulet, A. Greiser, J. K. Mendes, C. McGann, G. Treiman, and D. L. Parker, "Highly accelerated cardiac cine phasecontrast MRI using an undersampled radial acquisition and temporally constrained reconstruction," *J. Magn. Reson. Imag.*, 2013.

[26] A. Joseph, K. Merboldt, D. Voit, S. Zhang, M. Uecker, J. Lotz, and J. Frahm, "Real-time phase-contrast MRI of cardiovascular blood flow using undersampled radial fast low-angle shot and nonlinear inverse reconstruction," *NMR Biomed.*, vol. 25, pp. 917–924, Jul. 2012.

[27] C. Santelli, T. Schaeffter, and S. Kozerke, "Radial k-t spirit: Autocalibrated parallel imaging for generalized phase-contrast MRI," *Magn. Reson. Med.*, Nov. 2013.

[28] Y. Tao, G. Rilling, M. Davies, and I. Marshall, "Carotid blood flow measurement accelerated by compressed sensing: Validation in healthy volunteers," *Magn. Reson. Imag.*, vol. 31, no. 9, pp. 1485–1491, Nov. 2013.

[29] J. Hutter, P. Schmitt, G. Aandal, A. Greiser, C. Forman, R. Grimm, J. Hornegger, and A. Maier, "Low-rank and sparse matrix decomposition for compressed sensing reconstruction of magnetic resonance 4-D phase contrast blood flow imaging (LoSDeCoS 4-D-PCI)," in *16th International Conference for Medical Image Computing and Computer-Assisted Intervention (MICCAI 2013)*, K. Mori, I. Sakuma, Y. Sato, C. Barillot, and N. Navab, Eds. New York: Springer, 2013, vol. 8149, Lecture Notes in Computer Science, pp. 558–565.

[30] J. Hutter, A. Greiser, R. Grimm, C. Forman, J. Hornegger, and P. Schmitt, "Multi-dimensional flow-adapted compressed sensing (MDFCS) for time-resolved velocity-encoded phase contrast MRA," in *Proc. 10th IEEE Int. Symp. Biomed. Imag.*, San Francisco, CA, 2013, pp. 13–16.

[31] N. J. Pelc, M. A. Bernstein, A. Shimakawa, and G. H. Glover, "Encoding strategies for three-direction phase-contrast MR imaging of flow," *J. Magn. Reson. Imag.*, vol. 1, no. 4, pp. 405–413, Jul./Aug. 1991.

[32] P. Chai and R. Mohiaddin, "How we perform cardiovascular magnetic resonance flow assessment using phase-contrast velocity mapping," *J. Cardiovasc. Magn. Reson.*, vol. 7, no. 4, pp. 705–716, Jan./Dec. 2005.

[33] J. Hutter, R. Grimm, C. Forman, J. Hornegger, and P. Schmitt, "Inverse root sampling pattern for iterative reconstruction in non-CE MR angiography," in *Proc. Annu. Conf. ESMRMB*, Leipzig, Germany, Oct. 6–8, 2011.

[34] P. B. Roemer, W. A. Edelstein, C. E. Hayes, S. P. Souza, and O. M. Mueller, "The NMR phased array," *Magn. Reson. Med.*, vol. 16, no. 2, pp. 192–225, Nov. 1990.

[35] F. Nocedal, "Updating quasi-newton matrices with limited storage," *Math. Computat.*, vol. 35, no. 151, pp. 773–782, Jul. 1980.

[36] L. Feng, R. Otazo, H. Jung, J. Jensen, J. Ye, D. Sodickson, and D. Kim, "Accelerated cardiac t2 mapping using breathhold multiecho fast spin-echo pulse sequence with k-t focuss," *Magn. Reson. Med.*, vol. 65, no. 6, pp. 1661–1669, 2011.

[37] Z. Wang, A. Bovik, H. Sheikh, and E. Simoncelli, "Image quality assessment: From error visibility to structural similarity," *IEEE Trans. Image Process.*, vol. 13, no. 4, pp. 600–612, Apr. 2004.

[38] Q. Long, X. Y. Xu, K. V. Ramnarine, and P. Hoskins, "Numerical investigation of physiologically realistic pulsatile flow through arterial stenosis," *J. Biomech.*, vol. 34, no. 10, pp. 1229–1242, Oct. 2001.

[39] S. Ringgaard, S. Oyre, and E. Pedersen, "Arterial MR imaging phase-contrast flow measurement: Improvements with varying velocity sensitivity during cardiac cycle," *Radiology*, vol. 232, no. 1, pp. 289–294, Jul. 2004.